Dissertations, Master's Theses and Master's Reports

2022

Hardware In The Loop Implementation and Simulations of a Wave Energy Converter using Typhoon HIL and Speedgoat

Pranav Nair
Michigan Technological University, ponair@mtu.edu

HARDWARE IN THE LOOP IMPLEMENTATION AND SIMULATIONS OF A

WAVE ENERGY CONVERTER USING TYPHOON HIL AND SPEEDGOAT

By

Pranav Nair

A REPORT

Submitted in partial fulfillment of the requirements for the degree of

MASTER OF SCIENCE

In Electrical Engineering

MICHIGAN TECHNOLOGICAL UNIVERSITY

2022

This report has been approved in partial fulfillment of the requirements for the Degree of MASTER OF SCIENCE in Electrical Engineering.

Department of Electrical and Computer Engineering

Report Advisor: *Dr. Wayne W. Weaver*

Committee Member: *Dr. Gordon G. Parker*

Committee Member: *Prof. John T. Lukowski*

Department Chair: *Dr. Glen E. Archer*

Contents

List of Figures

List of Tables

Acknowledgments

It has been exhilarating and challenging to pursue a Master's degree at the Michigan Technological University. It encouraged me to push past my limits and gave me a whole new perspective on approaching and solving challenges. Several people were instrumental in my success.

First and foremost, I extend my sincere gratitude to my advisor Dr. Wayne W. Weaver, for his patience throughout the process, leading me through this process, providing me with all the resources and believing in my abilities. I would also like to thank my committee members, Dr. Gordon G. Parker and Prof. John T. Lukowski, for taking out the time and effort to improve my work.

Finally, I owe a debt of gratitude to all of my friends, family, and teachers for their unwavering support in all of my decisions.

List of Abbreviations

MRES	Marine Renewable Energy Sources
WEC	Wave Energy Converter
HIL	Hardware In the Loop
GWh	Gigawatt hour
TWh/yr	Terawatt hour per year
MW	Megawatts
AC	Alternating Current
DC	Direct Current
PTO	Power Take-Off
ESS	Energy Storage System
PWM	Pulse Width Modulation
RL	Resistor-Inductor
RC	Resistor-Capacitor
AWG	American Wire Gauge
PD	Proportional-Derivative
PI	Proportional-Integral
DC	Duty Cycle
I/O	Input-Output

PC   Personal Computer

USB   Universal Serial Bus

SCADA   Supervisory Control and Data Acquisition

IDE   Integrated Development Environment

w.r.t   with respect to

τ_{ff} update rate

Abstract

Several studies have indicated that electricity production is the prime source of greenhouse emissions, more than flying and driving combined. Hence, over the past few decades, there has been a significant rise in the need for clean energy to achieve the targets in emissions reduction. It has been observed that the share of renewable energy sources in the percentage of total electricity production is rising, but, according to climate experts, the transition needs to speed up. Hence, it is significant to study and develop underutilized renewable energy sources.

One of these underutilized renewable energy sources is wave energy. It has been observed that wave energy is a source with very high potential and predictability but has been in the nascent development stage for a while now due to several technical challenges. One of them is the limitation in studying all the real-world scenarios in a laboratory and the cost of up-scaling it to the real world. A low-cost, efficient solution to study and validate such technologies is Hardware In the Loop (HIL) implementation.

In this study, an attempt has been made to develop a systematic wave energy converter (WEC) model using Typhoon HIL and Speedgoat. The developed model can act as a universal model to pick, study, test, and validate the individual components

of the WEC in the HIL environment. Preliminary results show a reasonable trend in the behavior of the WEC. WEC system behavior for both single and multi-frequency wave tests has been discussed in the report. The stability/operating conditions for the current model configuration and a few insights on the energy storage system have also been discussed.

Chapter 1

Introduction

Renewable energy technologies are the future. As per the assessment by the International Renewable Energy Agency (IRENA), deploying renewable energy sources at a higher rate would bring down emissions by 90% by 2050 [1]. The global energy consumption in 2040 is predicted to be higher by 30% than the one in 2010 [2] hence; there is a constant need to develop and study the existing underutilized renewable energy sources.

One of these energy sources is the Marine Renewable Energy Sources (MRES), including both tidal and wave energy. It has been observed that MRES are one of the significant untapped energy sources with a theoretical potential of about 151300 TWh/yr [3]. Due to technical and economic difficulties, most of the projects in

this renewable energy sector have been small-scale demonstrations with a capacity of about 1 MW compared to other renewable energy technologies. However, compared to wave energy, using mature tidal turbine technologies, tidal energy extraction has been demonstrating higher reliability due to lower complexities in power extraction. It has surpassed a total generation of 60 GWh in 2020 [4].

The most significant technical challenge in WEC technology is conducting studies in a laboratory environment. The scenarios demonstrated in a laboratory are highly controlled compared to real-world scenarios. Considering the economic challenges to up-scale a laboratory tested WEC technology to the real world with several unpredictable scenarios, the capital, time, and resources required are very high [5]. An economically viable and technically accurate option to tackle these challenges is implementing, testing, and validating these systems using HIL technologies.

The past few decades have seen an exponential rise in the available computational power. Hence, the use of simulations in testing the products has also increased. In parallel with this trend, using HIL devices with such simulations for rapid prototyping and validation of complex engineering systems has also seen a rise [6]. Various historical references to different kinds of HIL simulators used in flight testing, vehicle testing are available in the literature [7]. [8] defines a HIL simulator as "a setup that emulates a system by immersing faithful physical replicas of some of its subsystems

within a closed-loop virtual simulation of the remaining subsystems." Some advantages of HIL systems over other ways of product development are cost-effectiveness, repeatability, comprehensiveness, safety, and concurrent systems engineering [8].

For complex and expensive engineering systems like WECs, HIL simulations are highly appropriate. This study attempted to develop a systematic HIL model for a WEC. While modeling, the WEC system was segmented into individual mechanical, electrical, and control components. Segmenting the model makes studying individual components easier and implementing the improvements effortlessly into the large-scale model.

This report has been divided into three sections. The first part of the report explains the design process of the mechanical, electrical, and control subsystems for the WEC. Secondly, the report details the setup of the HIL devices and the model implementation, testing, and data acquisition using Typhoon HIL and Speedgoat devices. The final part of the report is focused on the analysis and discussions of the acquired data.

Chapter 2

Design

The basic structure of a wave energy conversion setup is shown in Figure 2.1.
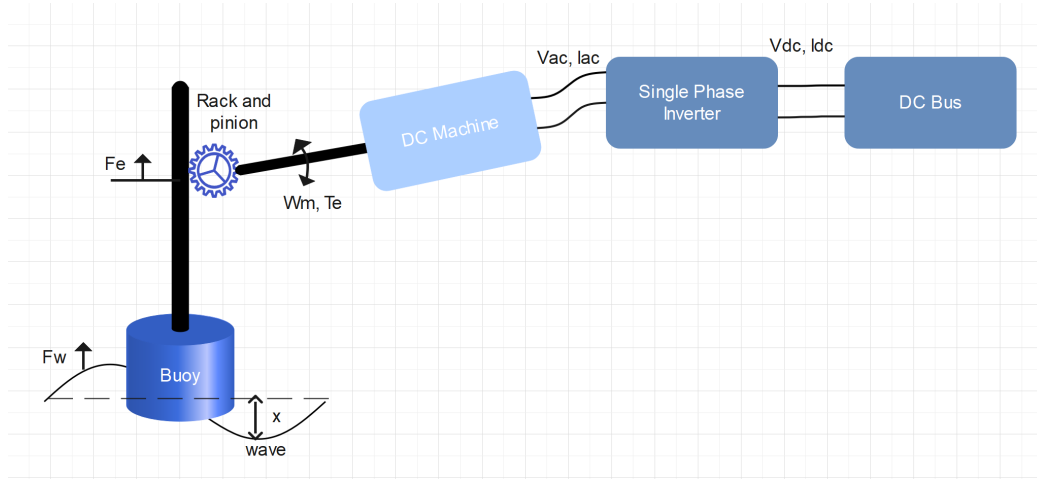
Figure 2.1: Basic structure of a wave energy conversion setup

The wave force generates a vertical linear motion of the buoy. This vertical linear motion is then converted into a rotational motion by a rack and pinion gear system.

This rotational motion in terms of motor speed/torque acts as a load to the DC machine. Then, the machine generates AC power, then converts it to DC power through a single-phase inverter.

2.1 Mechanical Systems

2.1.1 Buoy

The buoy has been modeled as a simple mass-spring-damper system for this study. The equation of motion for this system is shown as

$$\Sigma F = M\ddot{x} + C\dot{x} + Kx. \tag{2.1}$$

The forces considered in the system are the wave force $(\text{F}_w(\Omega))$, where Ω is the wave frequency and the actuator force (F_e). Substituting these terms into 2.1, the result is

$$F_w(\Omega) + F_e = M\ddot{x} + C\dot{x} + Kx. \tag{2.2}$$

where, x (m) is the position of the buoy, $\dot{x}$ (m/s) is the velocity of the buoy and $\ddot{x}$

(m/s^2) is the acceleration of the buoy. The values considered for the mass-spring-damper coefficients for this study are shown in Table 2.1.

Table 2.1
Mass-spring-damper parameter values

Parameter	Description	Value
M	Mass of the buoy	268 kg
C	Damper coefficient	1226 Ns/m
K	Spring constant	1194 N/m

2.1.2   Rack and Pinion

The rack and pinion gearing system converts the vertical linear motion of the buoy to rotational motion. Gear radius is an important parameter when translating the linear velocity into rotational velocity. This process is governed by

$$\dot{x} = v = r\omega_m. \tag{2.3}$$

This study has not considered the static and viscous friction losses in the rack and pinion gear system. The gear radius was considered to be 0.047 m. The gearing system can be sized using the values of the maximum linear and the rotational velocity as

7

$$r = \frac{\dot{x}_{max}}{\omega_{m,max}} = \frac{v_{max}}{\omega_{m,max}}. \tag{2.4}$$

where, r (m) is the gear radius, v and $\dot{x}$ (m/s) is the velocity of the buoy, $\dot{x}_{max}$ and v_{max} (m/s) is the maximum velocity of the buoy, ω_m (rad/s) is rotational speed of the DC machine and $\omega_{m,max}$ (rad/s) is the maximum rotational speed of the DC machine.

2.2 Electrical Systems

2.2.1 DC Machine

The DC machine model available in Typhoon HIL library is a separately excited DC machine, and this model has been used in this study [9]. The model schematic as seen in the Typhoon HIL Schematic editor can be seen in the Figure 2.2. F1 and F2 are the field (stator) winding terminals, and A1 and A2 are the armature (rotor) field windings.

The system of equations governing the electrical part of the DC machine is shown below in the (2.5), (2.6), (2.7) and (2.8). The electrical parameters represented with the subscript a indicate the armature part, and those with the subscript f indicate the field part of the DC machine. The armature and field voltage is computed as

8
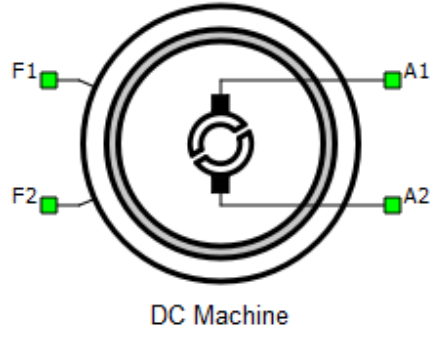
Figure 2.2: Typhoon HIL DC machine schematic

$$
\begin{bmatrix} v_a \\ v_f \end{bmatrix} = \begin{bmatrix} R_a & 0 \\ 0 & R_f \end{bmatrix} \begin{bmatrix} i_a \\ i_f \end{bmatrix} + \frac{d}{dt} \begin{bmatrix} \psi_a \\ \psi_f \end{bmatrix} + \begin{bmatrix} \omega_r \psi \\ 0 \end{bmatrix}. \tag{2.5}
$$

The armature and field winding flux can be computed as

$$
\begin{bmatrix} \psi_a \\ \psi_f \end{bmatrix} = \begin{bmatrix} L_a & 0 \\ 0 & L_f \end{bmatrix} \begin{bmatrix} i_a \\ i_f \end{bmatrix}. \tag{2.6}
$$

The motor flux linkage is governed by

$$
\psi = L_{af} i_f. \tag{2.7}
$$

The electrical torque of the machine is given by

9

$$T_e = \psi i_a. \tag{2.8}$$

The parameter values used for the electrical parameters of the DC machine were computed using (2.5), (2.6), (2.7), (2.8) and are given in Table 2.2.

Table 2.2
DC machine electrical parameters

Parameter	Description	Value
R_a	Armature winding resistance	0.01 Ω
R_f	Field winding resistance	25 Ω
L_a	Armature winding inductance	0.01 H
L_f	Field winding inductance	0.01 H
L_{af}	Mutual inductance between the armature and field windings	0.165 H
V_f	Field voltage	150 V

The motion equation for the mechanical part of the DC machine is such that

$$\frac{d\omega_m}{dt} = \frac{1}{J_m}(T_e - T_l - b\omega_m) \tag{2.9}$$

and

$$\theta_m = \int \omega_m dt. \tag{2.10}$$

The parameter values used for the mechanical parameters of the DC machine are shown in Table 2.3.

Table 2.3
DC machine mechanical parameters

Parameter	Description	Value
Jm	Combined rotor and load moment of inertia	0.02215 kg.m^2
b	Machine viscous friction coefficient	0 Nms
Unconstrained mechanical angle	Limiting mechanical angle between 0 and 2π	disabled

The following important parameter in the DC machine setup is the load applied to the machine. Typhoon HIL gives the load to the motor through the model or an external pin. This study applied a speed load to the motor from the model environment. Figure 2.3 shows how the motor load parameter was set up in the Typhoon HIL Schematic Editor.
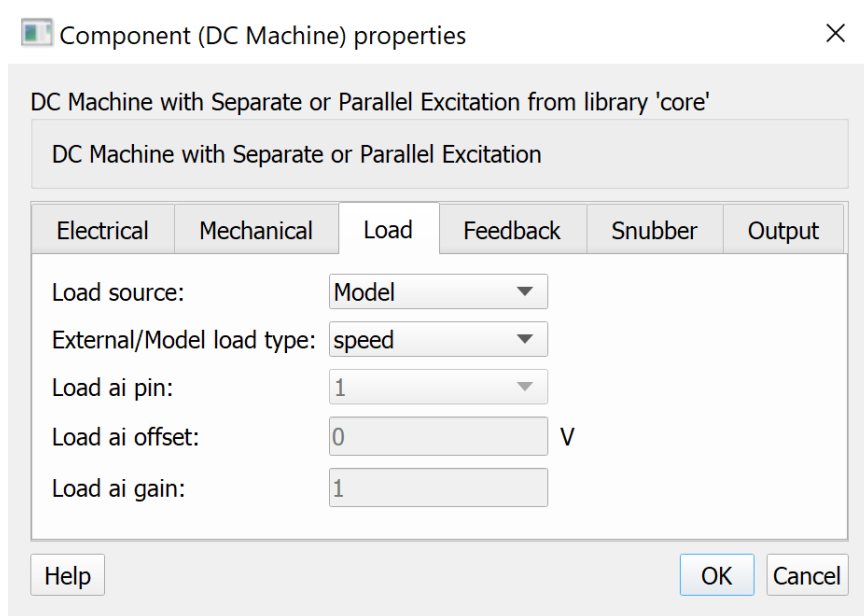
Figure 2.3: Typhoon HIL DC machine load parameter

2.2.2 Power Electronics - Single Phase Inverter

A single-phase inverter is used to convert the AC power to DC power in this system. The single-phase inverter model available in the Typhoon HIL library has been used in this study [9]. The switches and diodes used in this model are ideal, and the losses are not considered. The model schematic as seen in the Typhoon HIL Schematic editor can be seen in the Figure 2.4. The general internal representation of a single-phase inverter as shown in [9] can also be seen below in Figure 2.5.
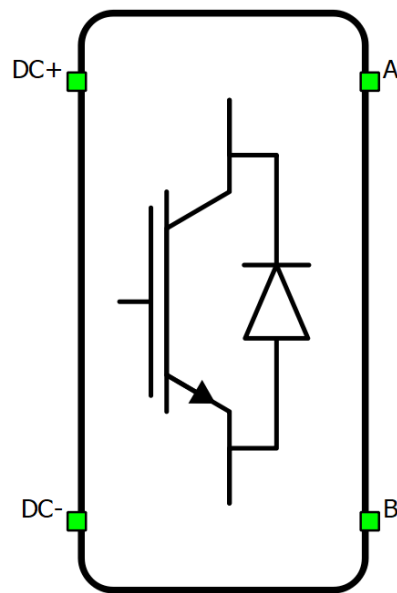
Figure 2.4: Typhoon HIL single phase inverter schematic

There are multiple options available in Typhoon HIL to control the inverter module. The first option is to provide switching signals to the individual inverter switches/legs through external hardware and pins. Another option is using the internal modulator
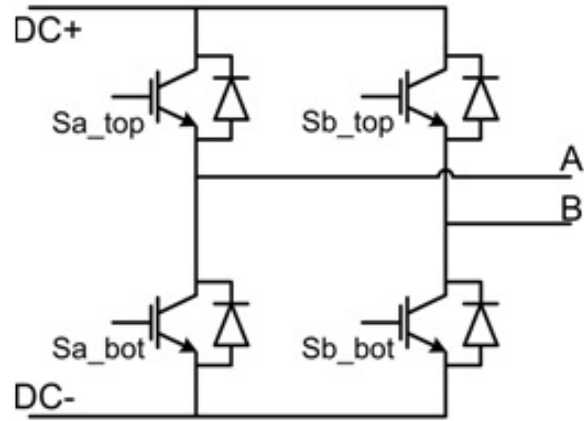
Figure 2.5: Single phase inverter general representation

to modulate the PWM switching signals based on the reference signals provided through the model. This study uses the latter, and the generation of the reference signals is explained in section 2.3.2.

The inverter set up for this study is seen in Figure 2.6. An internal modulator was used to generate the PWM switching signals based on the reference signal in the range of 0-1. This means that when the reference signal is 0.5, both the legs of inverter switches conduct for 50% of the time period (duty cycle of 50%). All the other parameters are discussed in detail under PWM modulator in [9].
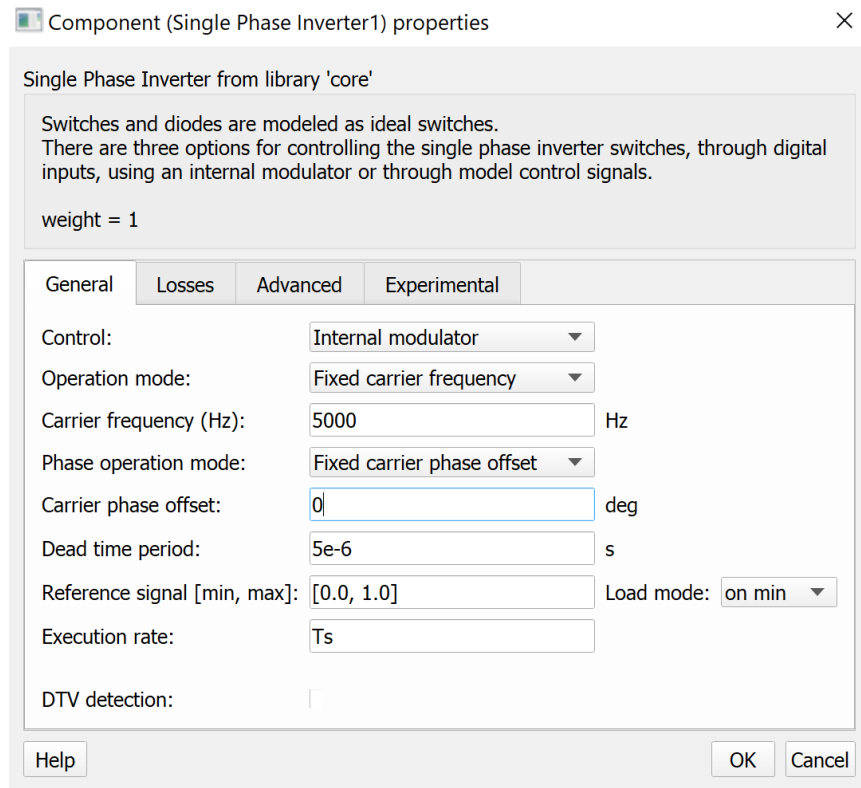
Figure 2.6: Single phase inverter setup for the study

2.2.3 Energy Storage System and Power Take-Off to the Grid

The basic structure of the WEC as shown in Figure 2.1 is simplified and does not include the power take-off to the grid. However, designing the power take-off is very important to study the scope of a renewable energy source. The design for power take-off is incorporated from [10]. The design for power take-off can be seen in Figure 2.7.
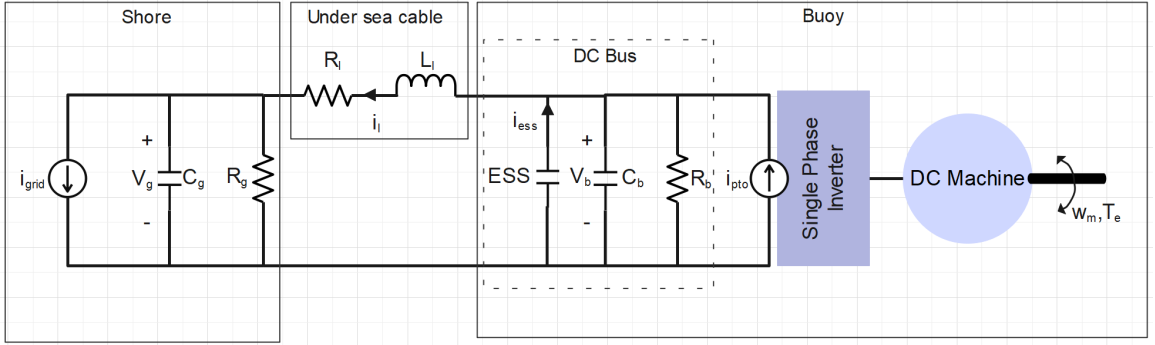
Figure 2.7: ESS and PTO to the grid

The model of the system for power take-off is shown

$$C_b \frac{dV_b}{dt} = i_{pto} - \frac{V_b}{R_b} - i_{ess} - i_l. \tag{2.11}$$

$$L_l \frac{di_l}{dt} = V_b - i_l R_l - V_g. \tag{2.12}$$

$$C_g \frac{dV_g}{dt} = i_l - i_{grid} - \frac{V_g}{R_g}. \tag{2.13}$$

The model variables and the parameter values used are shown in the Tables 2.4 and 2.5 respectively [10].

Table 2.4
Parameters for the ESS and PTO circuit model

Parameter	Description	Value
R_b	Bus Parasitic Resistance	1000 Ω
R_g	Grid Inverter Resistance	1000 Ω
C_b	Bus Capacitance	2 μF
C_g	Grid Inverter Capacitance	2 μF
R_l	Under sea cable inductance	2.5 Ω
L_l	Under sea cable inductance	95.6 μH

Table 2.5
Variables for the ESS and PTO circuit model

Parameter	Description
i_{pto}	Current from the WEC drive (A)
i_{ess}	Current from the ESS (A)
i_{grid}	Current drawn into the grid (A)
i_l	Current in the under sea cable (A)
V_b	Bus voltage (V)
V_g	Grid-side voltage (V)

ESS requirements for the WEC system are relatively small [10]. Passive supercapacitor systems can act as the ESS. Having a supercapacitor bank on the buoy also helps in direct filtering of the DC power, and an active DC-DC converter is not required [10]. In [10], the ESS has been emulated as a current source with PI control which assumes that the ESS has infinite energy to stabilize the bus, but, in this study, a supercapacitor model available in the Typhoon HIL library has been used [9]. This

can provide a better overview of how the ESS would behave in the WEC system.

The undersea cable used to transmit the power from the buoy to the shore has been modeled as a series RL circuit. A 6 AWG, 1 km cable has been considered. The equations governing the parameter design for the undersea cable can be seen in (2.14) and (2.15) [11].

$$L_l = \frac{\mu_o \mu_r}{\pi} \cosh^{-1}\left(\frac{s}{d}\right) (length\, of\, the\, cable). \tag{2.14}$$

$$R_l = (DC\, resistance\, of\, the\, cable)\,(length\, of\, the\, cable)\,(2). \tag{2.15}$$

where the values of the parameters used to compute L_l and R_l shown in Table 2.4 are, permeability of free space ($\mu_o = 4\pi e^{-7}$ H/m), relative permeability ($\mu_r = 1$ H/m), distance between the conductors (s = 4.115 mm), diameter of the conductors (d = 4 mm), length of the cable = 1 km = 1000 m, DC resistance of a 6 AWG copper cable = 1.25 mΩ/m.

A grid side inverter has been realized using an RC circuit on the shore side. The power injected into the grid is emulated by a current source i_{grid}. There is a specific control structure implemented to update the power command to the grid through

changing the reference i_{grid} current value. It has been explained in detail in section 2.3.3.

2.3 Controls

2.3.1 PD control to maximize the wave power extraction

A PD control is implemented for the actuator force (F_e) to generate an F_{eref} such that maximum power is extracted from the wave force ($F_w(\Omega)$) [12]. The equation governing this control is shown

$$F_{e,ref} = -k_{p,pd}x - k_{d,pd}\dot{x}.$$ (2.16)

The gains were computed to match the impedance of the system as

$$k_{p,pd} = M\Omega^2 - K.$$ (2.17)

$$k_{d,pd} = C.$$ (2.18)

where, $k_{p,pd}$ is the proportional gain and $k_{d,pd}$ is the derivative gain used here. The values of M, C, and K used are given in Table 2.1.

2.3.2 Inverter control

Inverter control determines the modulation signal provided to the inverter. The modulation signal determines the switching of the inverter switches through the internal modulator. From the $F_{e,ref}$ computed in the PD control, using the gear radius, a reference torque is generated. The reference torque is compared with the present torque of the machine. Then, a control action is initiated through a PI controller to determine the modulation signal. The controller gains are tuned to be $k_{p,inv} = 0.01$ and $k_{i,inv} = 0.05$ by analyzing the error between the machine torque and the computed reference torque. The modulation signal is limited to a range of 0-1. The action of this control can be explained through (2.19) and (2.20).

$$\tilde{T}_e = T_{e,ref} - T_e. \tag{2.19}$$

$$Modulation\ signal = k_{p,inv}\tilde{T}_e + k_{i,inv}\int \tilde{T}_e dt. \tag{2.20}$$

where, $k_{p,inv}$ is the proportional gain and $k_{i,inv}$ is the integral gain.

2.3.3 Grid reference feed-forward control

The model variables used to design the control can be seen in Table.2.6. The reference bus voltage is set at 200 V during this study. As mentioned in section 2.2.3, the grid side on the shore is realized using a current source (i_{grid}) and an RC circuit. The power export from the WEC to the grid is performed through this control.

Table 2.6
Variables for the grid reference control model

Parameter	Description
i_{pto}	Current from the WEC drive (A)
$i_{l,ref}$	Reference undersea cable current (A)
$i_{g,ref}$	Reference grid current (A)
$V_{b,ref}$	Reference bus voltage (V)
$V_{g,ref}$	Reference grid voltage (V)

Continuously updating the power export command is ideal, but it poses challenges due to the inverter and communication difficulties. Hence, a concept of update rate (τ_{ff}) has been introduced. τ_{ff} is the rate at which the grid power export is updated through the update of reference grid current ($i_{g,ref}$). Basic Kirchoff's laws are used to compute the reference grid current. The process used to compute the reference grid current ($i_{g,ref}$) can be seen below [10].

Analyzing the circuit from the bus side to the shore side, a reference undersea cable

current is computed by reducing the bus side parasitic losses from the WEC drive current

$$i_{l,ref} = i_{pto} - \frac{V_{b,ref}}{R_b}. \tag{2.21}$$

Then, the grid side reference voltage is computed by reducing the undersea cable transmission voltage drop from the reference bus voltage

$$V_{g,ref} = V_{b,ref} - i_{l,ref} R_l. \tag{2.22}$$

On the grid side, the losses due to the grid side inverter resistance is reduced from the incoming undersea cable reference current to compute the reference grid current

$$i_{g,ref} = i_{l,ref} - \frac{V_{g,ref}}{R_g}. \tag{2.23}$$

Combining all the above equations as

$$i_{g,ref} = i_{pto}\left(1 + \frac{R_l}{R_g}\right) - V_{b,ref}\left(\frac{R_b + R_g + R_l}{R_b R_g}\right). \tag{2.24}$$

The update rate parameter τ_{ff} was realized using a zero-order hold. Zero order hold block is available in Simulink under Discrete library [13]. It was required that the grid demand was updated at a specific sample period. This block works as a switch which holds the current value for a specified sample period (update rate) and then updates it periodically. The effect and significance of τ_{ff} on the system behavior has been explained and illustrated in chapter 4.

Chapter 3

Hardware In the Loop

Implementation

HIL implementation of the WEC system was done using a Typhoon HIL 604 and two

baseline real-time target machines by Speedgoat. The mechanical part of the system

was implemented using Speedgoat 1, controls using Speedgoat 2 and the electrical part

using Typhoon HIL 604. A PC was used as a host PC to configure all the devices

and to view the testing panel. Speedgoat connects to the host PC via Ethernet and

the switch in the figure is the high speed NETGEAR Ethernet switch used to link

both the Speedgoat devices. The hardware rack setup used can be seen in Figure 3.1.
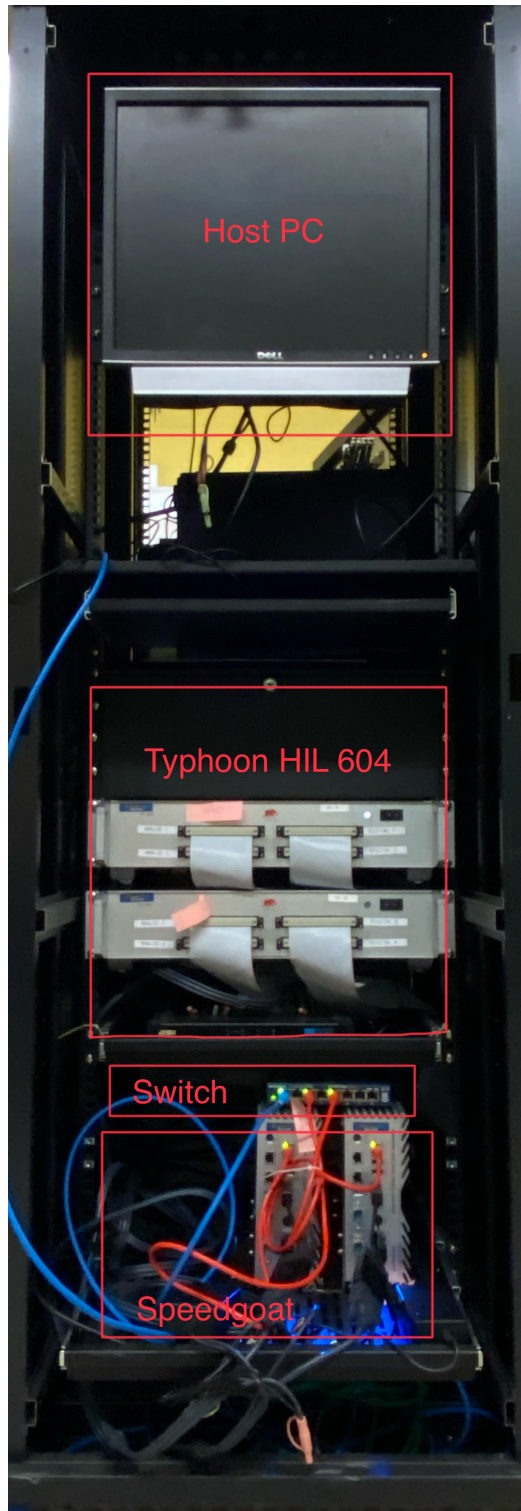
Figure 3.1: Hardware rack setup

Figure 3.2 shows the other side of the hardware rack and the breakout boards used to get the I/O's out of the hardware can be seen.
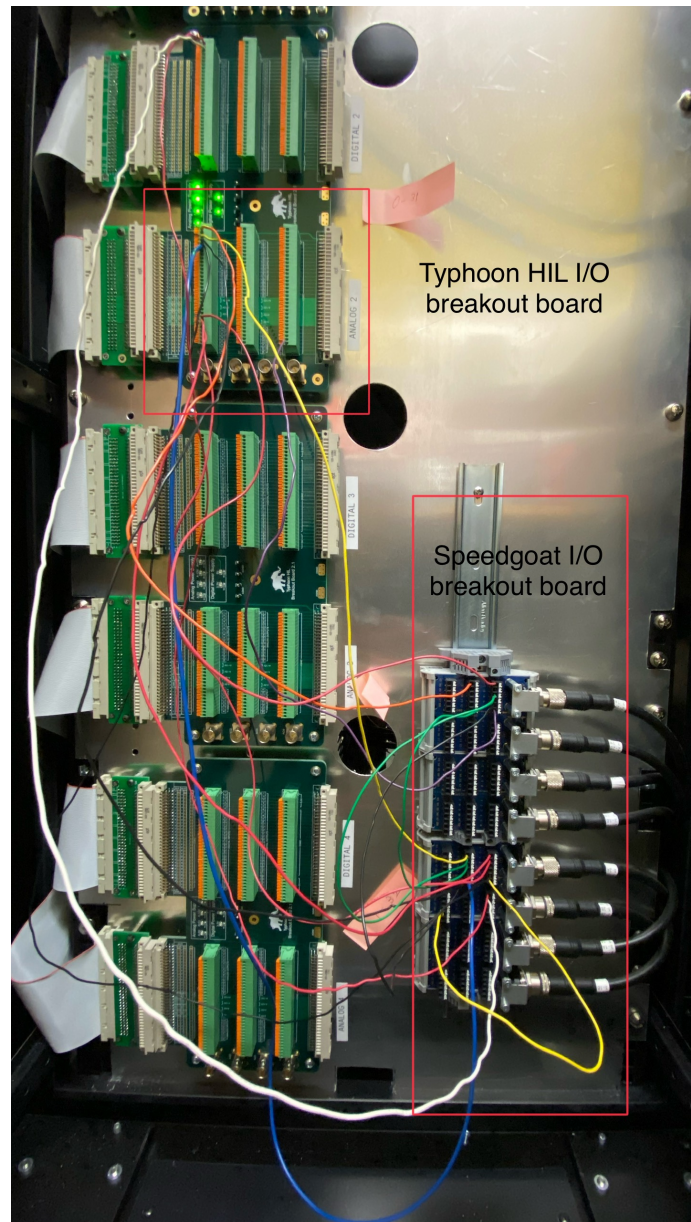

Figure 3.2: Hardware rack setup I/O's

Tables 3.1, 3.2 and 3.3 shows the details about wiring the I/O's for the hardware devices. All the parameter values were calibrated and counter-calibrated to appropriate analog voltage ranges mentioned below in the hardware description.

Table 3.1

Hardware I/O wiring - Speedgoat 1 - mechanical sub-system

I/O	Parameter	From/To
I	Machine Torque (T_e)	From Typhoon HIL 604
O	Load Speed (ω_m)	To Typhoon HIL 604
O	Position of the buoy (x)	To Speedgoat 2
O	Velocity of the buoy (v)	To Speedgoat 2

Table 3.2

Hardware I/O wiring - Speedgoat 2 - controls sub-system

I/O	Parameter	From/To
I	Machine Torque (T_e)	From Typhoon HIL 604
I	WEC drive current (i_{pto})	From Typhoon HIL 604
I	Position of the buoy (x)	From Speedgoat 1
I	Velocity of the buoy (v)	From Speedgoat 1
O	Modulation Signal	To Typhoon HIL 604
O	$i_{g,ref}$	To Typhoon HIL 604

Table 3.3

Hardware I/O wiring - Typhoon HIL 604 - electrical sub-system

I/O	Parameter	From/To
I	Modulation Signal	From Speedgoat 2
I	$i_{g,ref}$	From Speedgoat 2
I	Load Speed (ω_m)	From Speedgoat 1
O	Machine Torque (T_e)	To Speedgoat 1 and 2
O	WEC drive current (i_{pto})	To Speedgoat 2

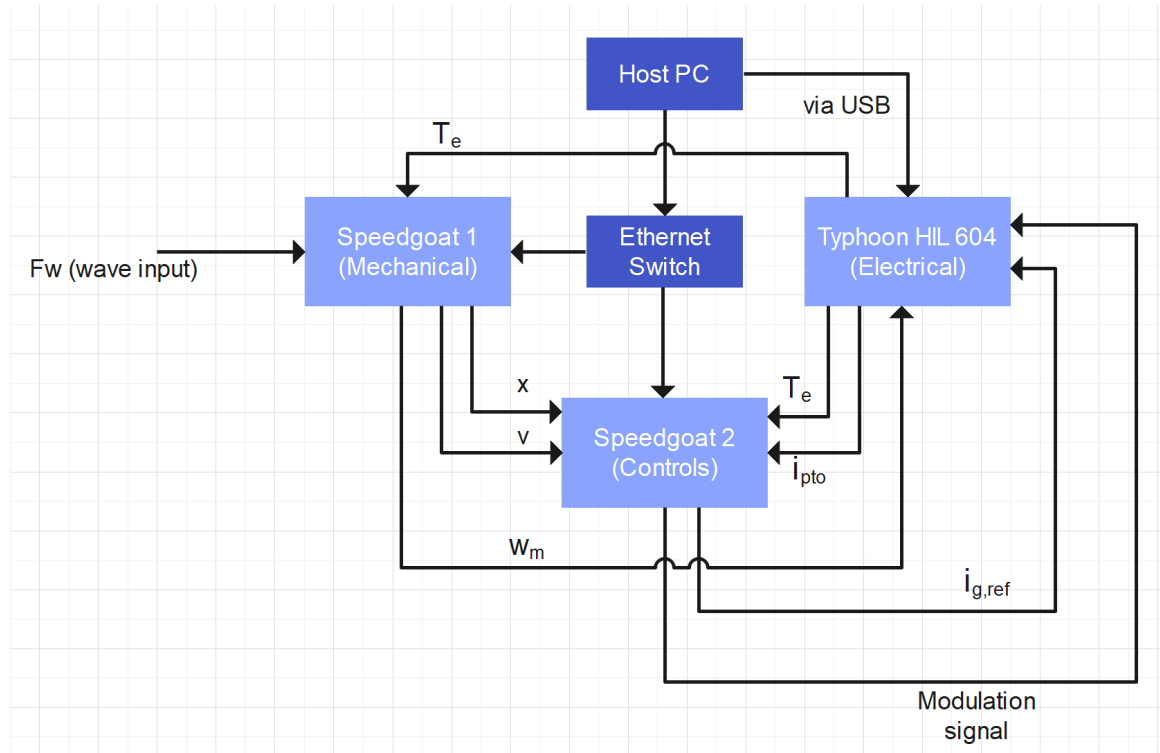Figure 3.3 shows the schematic of I/O's between the WEC subsystems.

Figure 3.3: I/O wiring schematic

3.1 Typhoon HIL

3.1.1 Hardware and Setup

Typhoon HIL focuses on the products and tools for power electronics testing and validation. The hardware used for this study is the Typhoon HIL 604 [9]. HIL breakout board is used in the setup to access the analog and digital I/O [9]. Analog

I/O was majorly used for this study. Analog I/O has a voltage range of ± 10 V. All the inputs quantities were counter-calibrated, and output quantities were calibrated such that the I/O electrical signals would stay within their limits.

Setting up a Typhoon HIL 604 is a relatively simple process. The hardware can be directly plugged into the host PC through a USB port. The PC detects the hardware, and the driver software is automatically installed [9].

3.1.2 Modeling Tools

Typhoon HIL Control Center is the interface used to launch Typhoon HIL tools. The tools majorly used for this study are Typhoon HIL Schematic Editor and HIL SCADA. Various other tools like the Typhoon Test IDE and Script editor can write Python-based automated tests for validating the models.

3.1.2.1 Typhoon HIL Schematic Editor

Typhoon HIL Schematic Editor is the modeling environment provided by Typhoon HIL and is one of the essential tools. It is intuitive and straightforward to use. It contains a library browser, as shown in Figure 3.4.
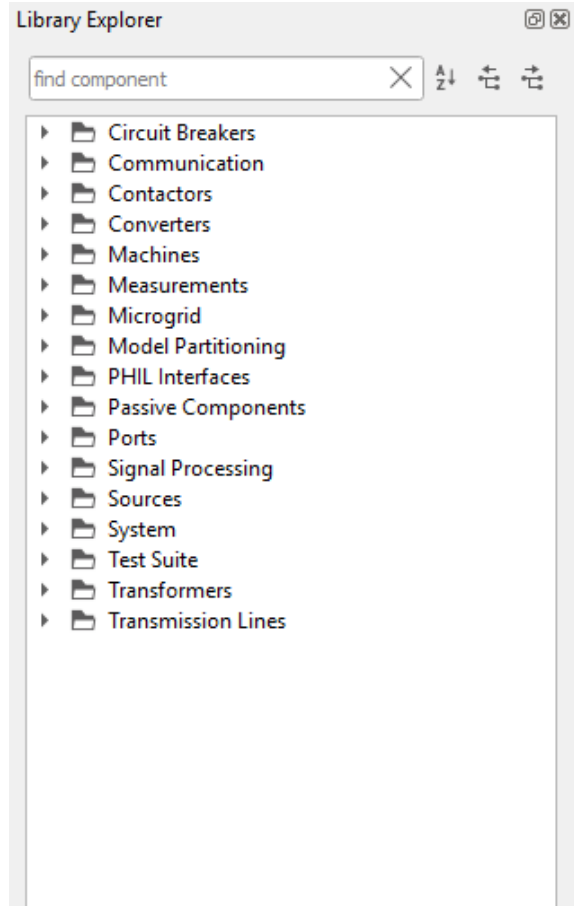
Figure 3.4: Typhoon HIL Library Browser

Any components required can be easily chosen, dragged, and dropped into the schematic. The right-most icon in the toolbar below the menu bar is a 'Compile and load in HIL SCADA' icon. This helps to compile the model and load it into HIL SCADA, which is the testing environment provided by Typhoon HIL [9]. A sample circuit built in the Typhoon HIL Schematic Editor environment can be seen in Figure 3.5.
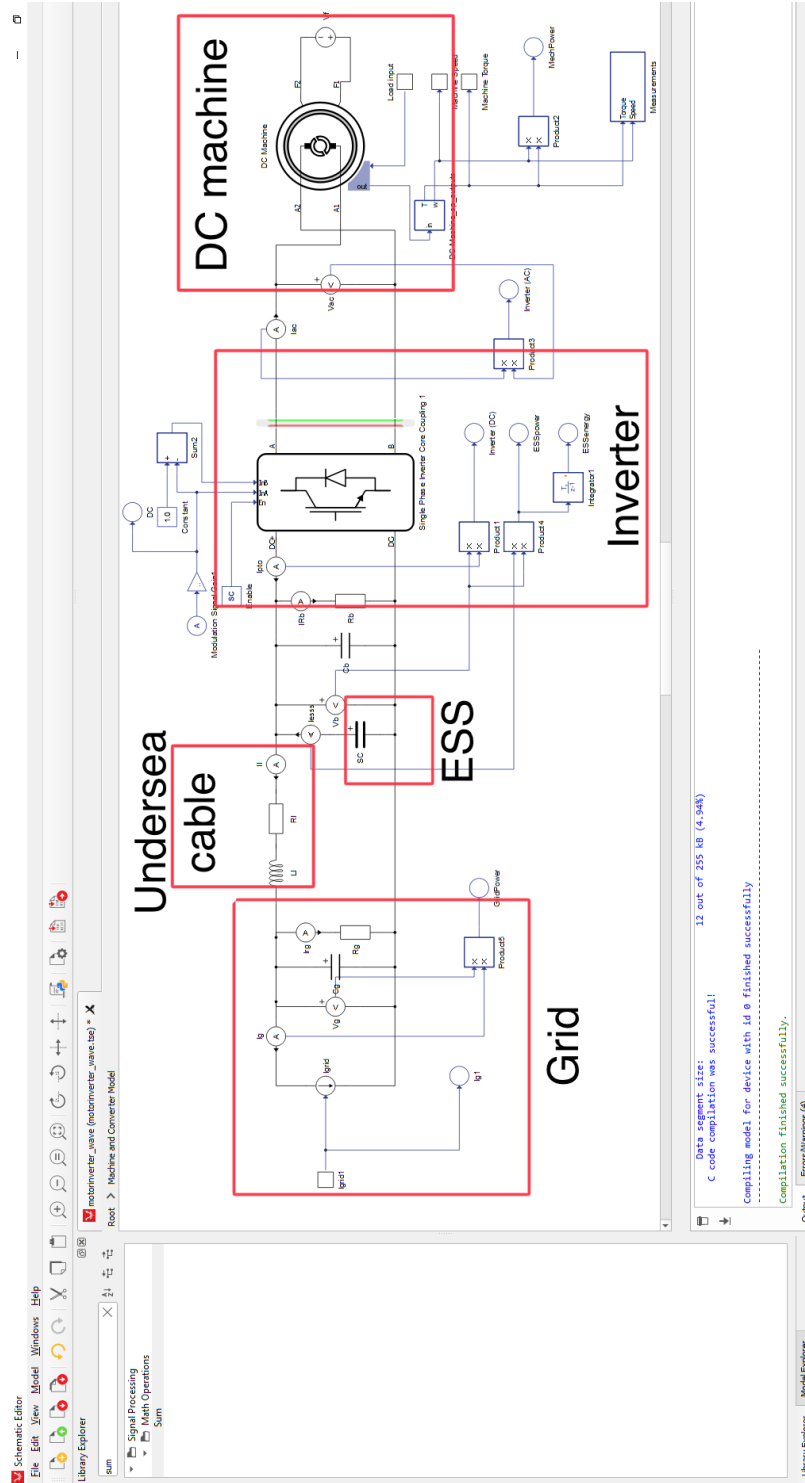
Figure 3.5: Typhoon HIL Schematic Editor environment

3.1.2.2 HIL SCADA

HIL SCADA is the tool used to design the testing panel to validate the model. Several visual tools are available in HIL SCADA to develop the testing panel. HIL SCADA also provides an interface through 'Model Settings' to access and configure all the external/internal hardware inputs and modify the modifiable model parameters like controller gains during the data run. After the compilation process, HIL SCADA also provides an option to test the model using 'Virtual HIL (VHIL)' if the hardware device is unavailable. Figure 3.6 shows the visual tools available and the testing panel used in this study.
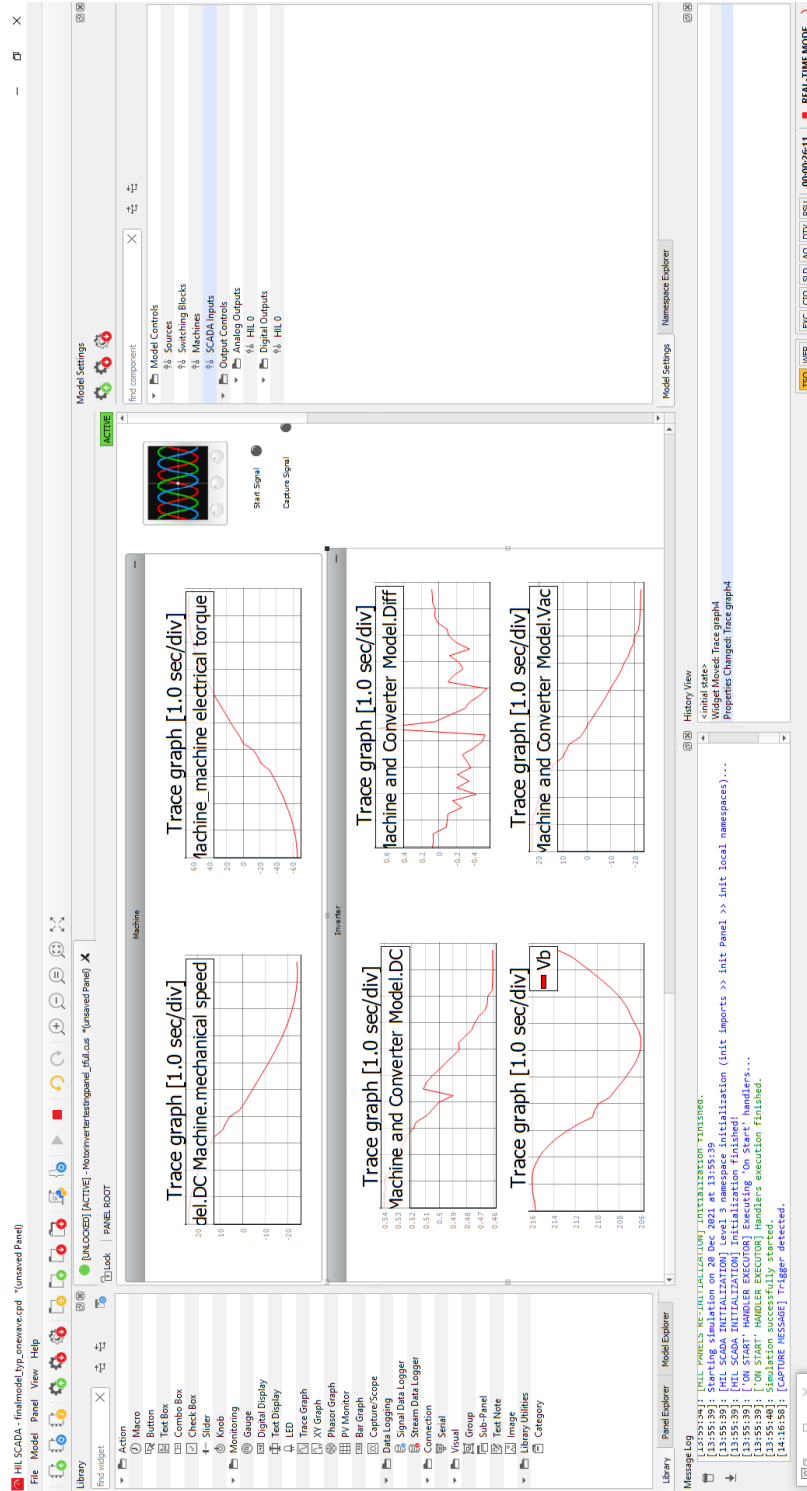
Figure 3.6: HIL SCADA testing panel

3.2   Speedgoat

The Speedgoat focuses on the solutions for HIL testing and validation. Speedgoat devices are designed to be used with Simulink and Simulink Real-time from Mathworks. As Simulink has an extensive library, Speedgoat can be used for a wide range of applications compared to Typhoon HIL.

3.2.1   Hardware and Setup

Two 'Baseline Real-Time Target Machines' were used during this study. One of the advantages of Speedgoat target machines is that they have I/O boards and specifications that can be assembled according to the purpose of the customer. Each target machine used in this study has two I/O boards assembled, namely IO183 and IO397. Analog I/O ports of the IO183 module were used during this study. The module has eight analog inputs with a voltage range of ± 10 V and four analog outputs that can be configured as either 0-2.5V or 0-5V. All the inputs quantities were counter-calibrated, and output quantities were calibrated such that the I/O electrical signals would stay within their limits.

Speedgoat setup is comparatively complicated as compared to Typhoon HIL.

The host PC should have MATLAB, Simulink, MATLAB and Simulink Coders, and Simulink Real-Time installed. Using Speedgoat involves building the model and code generation; hence, a required C-compiler version should be installed. The Speedgoat libraries for Simulink Real-Time should be installed. The models used for this study can be seen in Figure 3.7. The target machine should be powered. The Ethernet cable
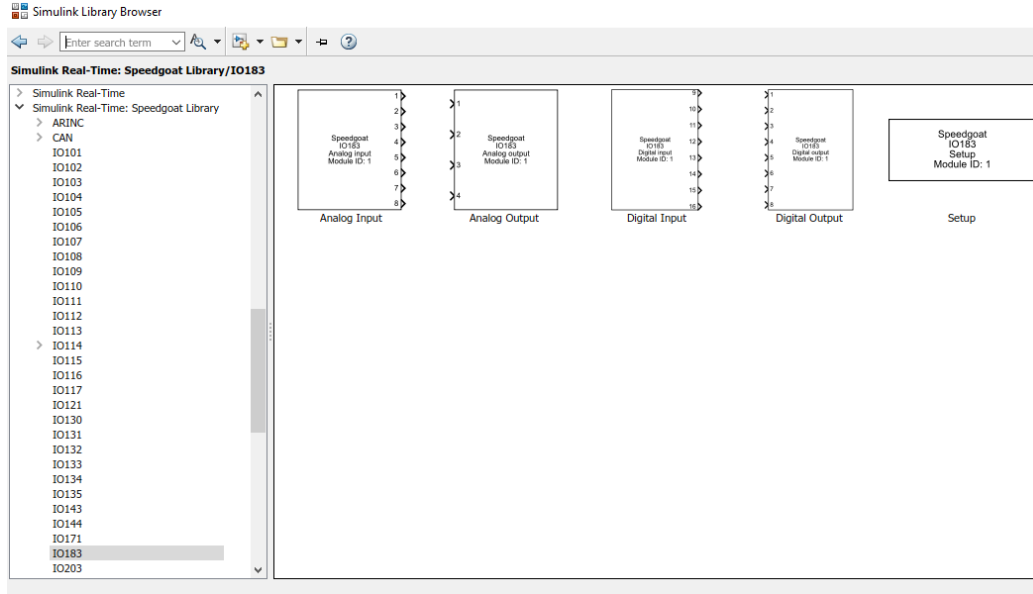

Figure 3.7: IO183 models from Simulink Real-Time library

should connect the target machine and the host PC. In this study, a NETGEAR high-speed ethernet switch has been used to establish the common connection between the Speedgoat devices. On the host PC, through the 'Network and Sharing Center,' the 'Internet Protocol Version 4' properties should be configured for Ethernet.On MATLAB, the target machines can be accessed using the 'slrtexplr' command. Then, the connection can be established by changing the 'Host to Target Communication' properties to the preconfigured target machine TCP/IP settings. The target can be

36

pinged using the 'ping' command to test the communication between the target and the host PC.

3.2.2 Modeling Tools

MATLAB was used to initialize the parameters for the Simulink models. It was also used to process and analyze the data captured through Typhoon HIL. Simulink was used to develop, compile and build the models. Simulink requires a few setup procedures before running real-time models, and they are setting the simulation mode to 'External' as shown in Figure 3.8. The right most icon is used to build the model.
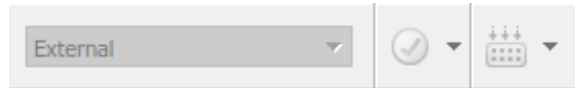
Figure 3.8: Simulation mode setup

Under the model configuration parameters, code generation settings and Simulink Real-Time options need to be setup. The target machine to build the model can be specified through these settings. Figures 3.9 and 3.10 shows the setup.
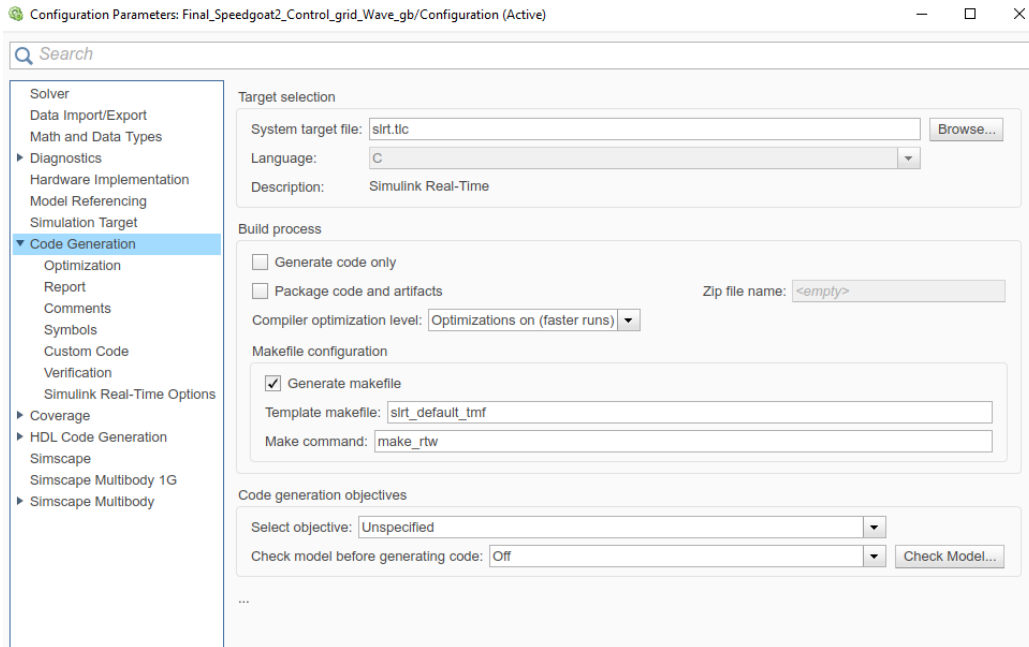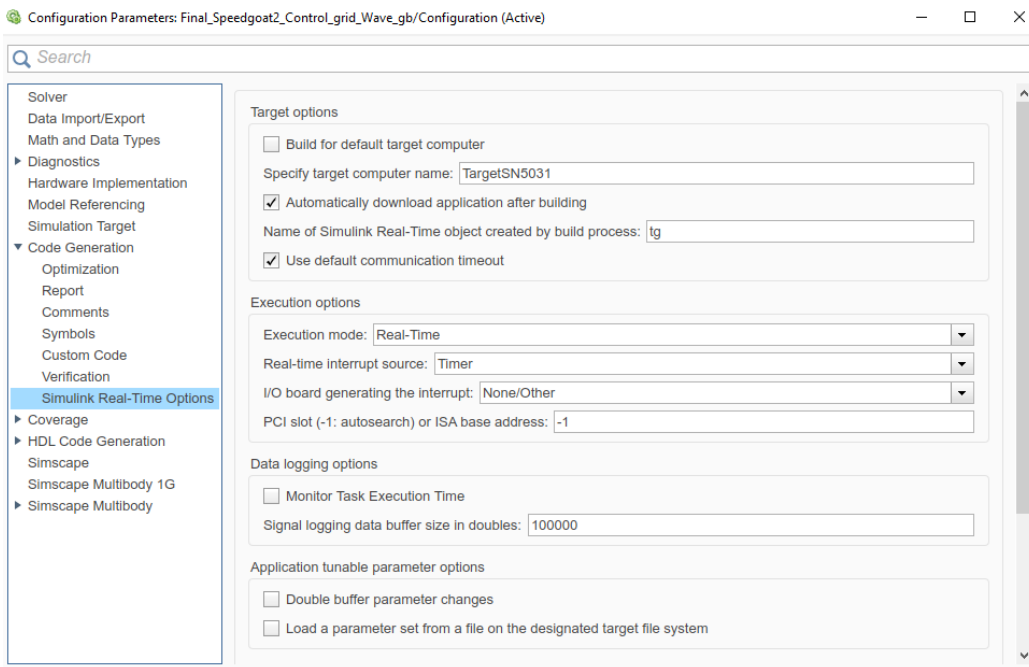
Figure 3.9: Model code generation settings

Figure 3.10: Model real-time target configuration settings

Chapter 4

Results and Discussions

4.1 Preliminary WEC model results

4.1.1 Single frequency wave test

The results presented in this section show the plots for all the essential WEC param-

eters for an update rate $\tau_{ff} = 1s$. The wave force is the only input to the model, and

for the presented case, wave force (F_w) is 5000 N and the wave period is 20 s.

Figure 4.1 shows the linear forces on the buoy. F_w is the wave input provided to the

system, and F_e is the actuator force. The actuator force is a reaction force to the

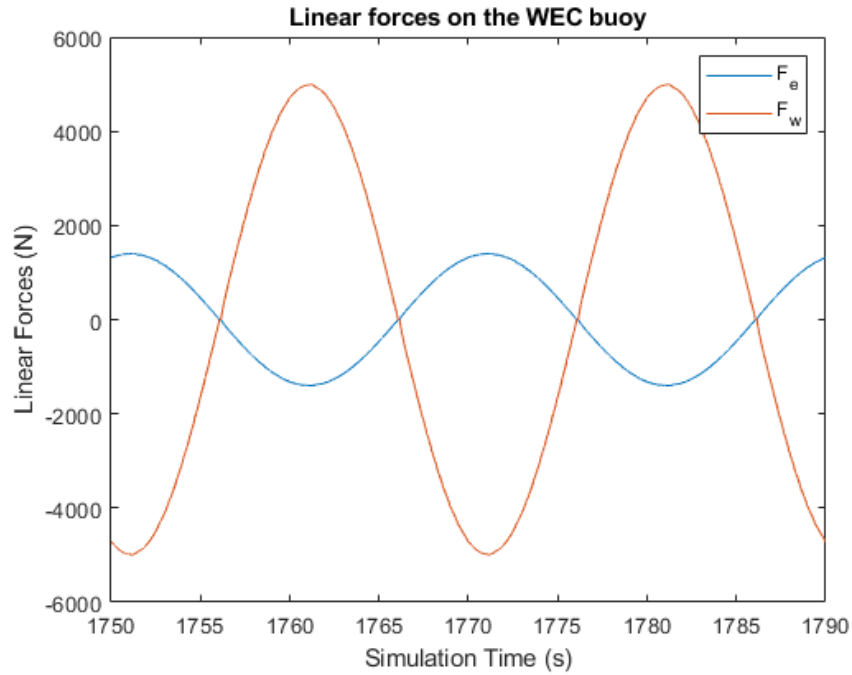wave input; hence, it is out of phase with the wave force.

Figure 4.1: Linear forces on the buoy - single frequency

Figures 4.2 and 4.3 show the vertical position and velocity of the buoy. From the reference, the buoy exhibits a vertical movement between 4 and -4 m. At the highest and lowest position, the velocity of the buoy becomes zero. The maximum velocity of the buoy was observed to be 1.15 m/s.
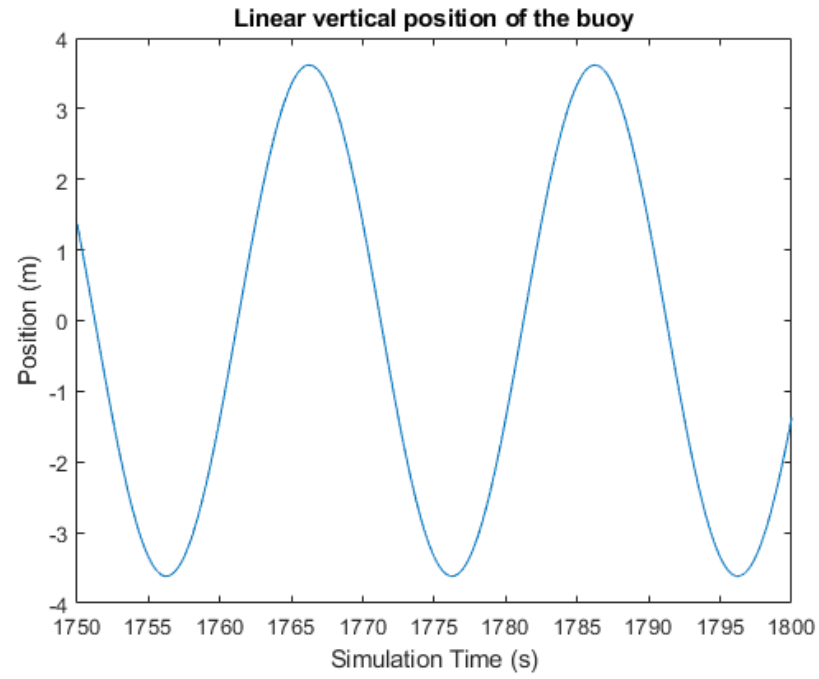
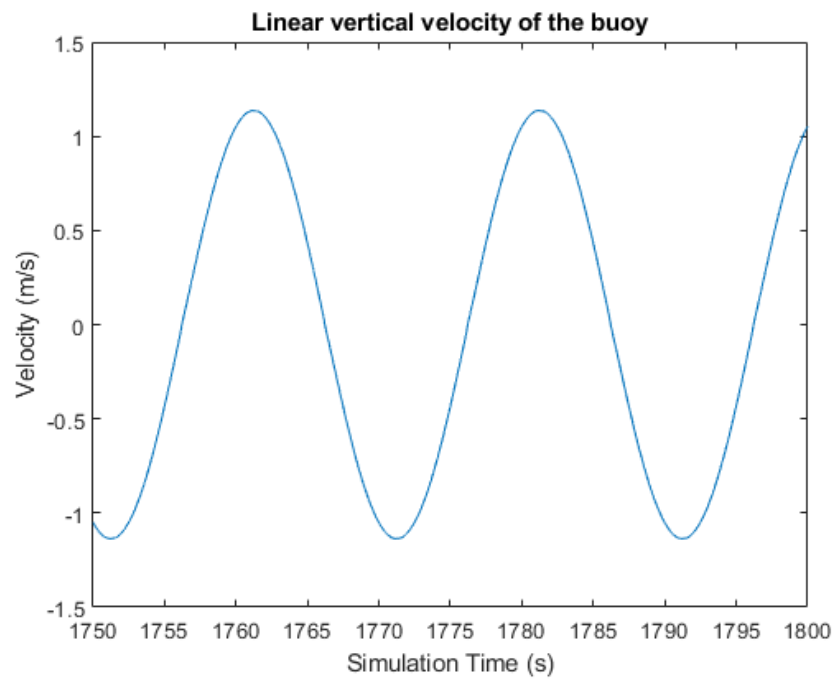**Figure 4.2:** Linear vertical position of the buoy - single frequency

Figure 4.3: Linear vertical velocity of the buoy - single frequency

The speed of the machine is shown in Figure 4.4. It can be validated using

$$\omega_m = \frac{Vertical\ velocity\ of\ the\ buoy}{Gear\ radius} = \frac{1.15}{0.047} = 24.46 rad/s. \qquad (4.1)$$
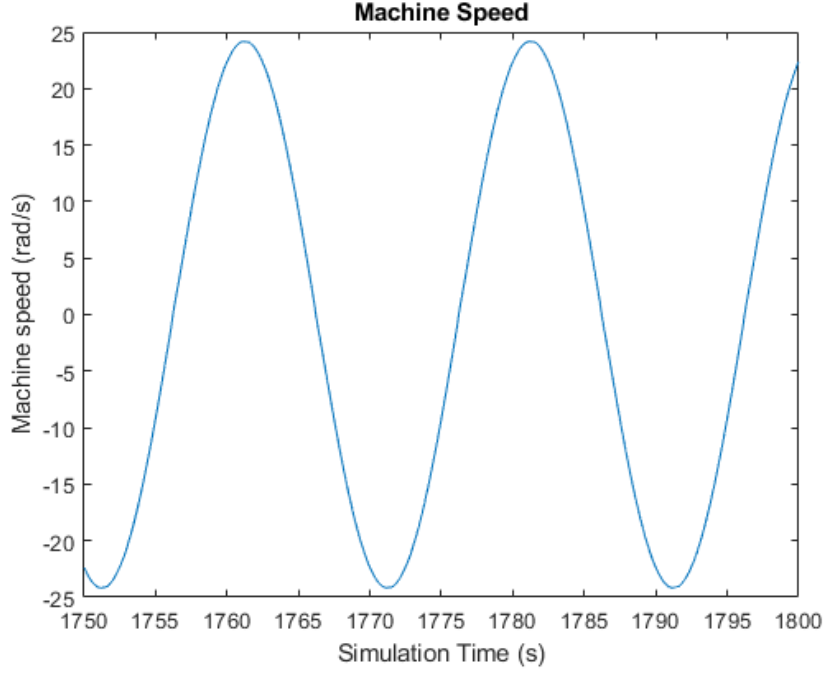

Figure 4.4: Speed of the DC machine - single frequency

The torque of the machine is generated through inverter PI control scheme (section 2.3.2). The reference torque generated through the reference actuator force $(F_{e,ref})$ as mentioned in section 2.3.1 can be seen in Figure 4.5. It can also be observed that the PI controller (section 2.3.2) does not have an error because the machine is achieving the reference torque.
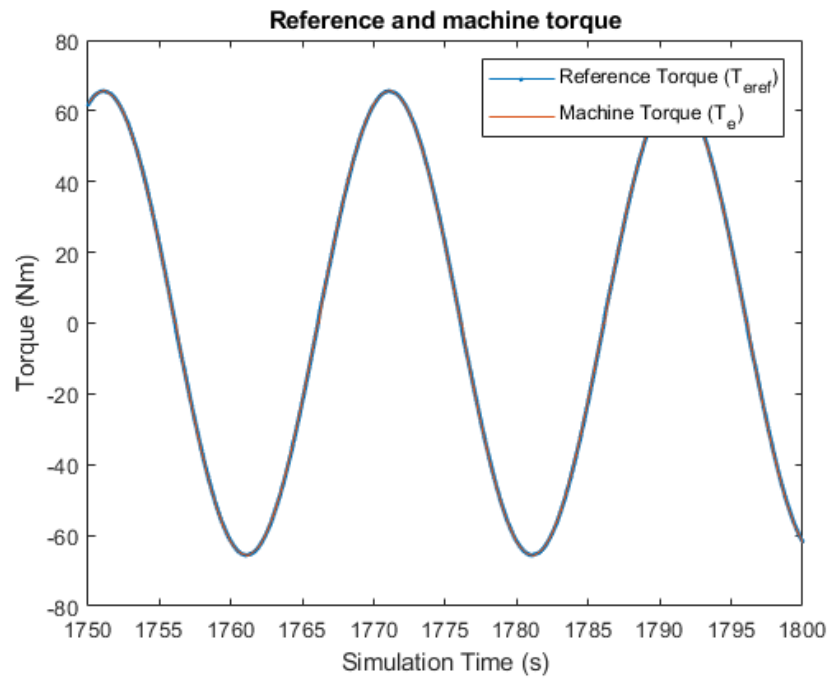
Figure 4.5: DC machine reference and actual torque - single frequency

Figure 4.6 shows the modulation signal generated by the PI controller (section 2.3.2) for the inverter control. It has an impact on the current from the WEC drive and the bus voltage.
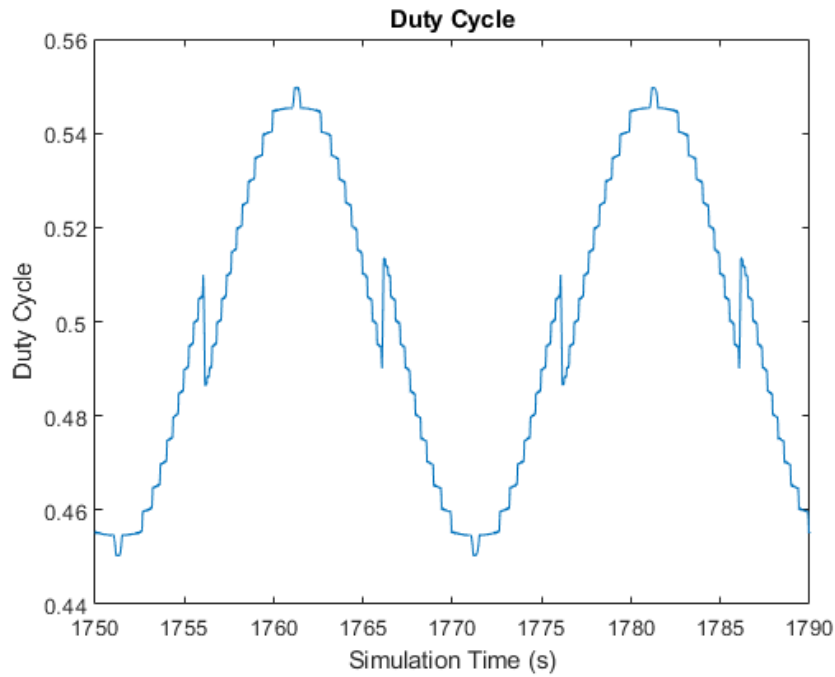

Figure 4.6: Modulation signal for inverter control - single frequency

The variation in the modulation signal is due to the variation in motor torque at zero. The torque transience is shown in Figure 4.7. But, as the variation stays for a time factor lower than 0.2 s and the controller catches up with the signal, the effect can be ignored.
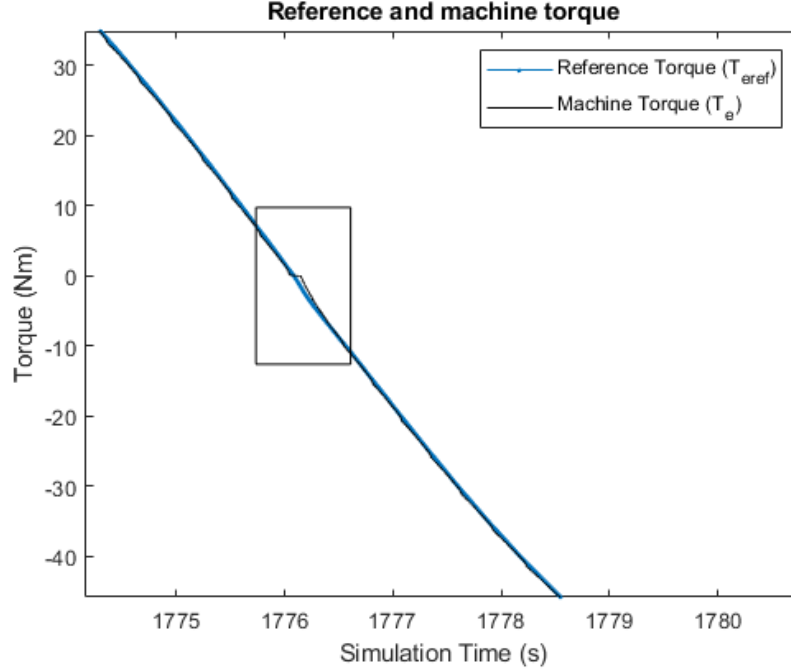
Figure 4.7: Torque variation

The current from the WEC drive is a significant parameter. The current from the WEC drive i_{pto} is shown in Figure 4.8 and it peaks at around 8 A for this case. The i_{pto} is always positive justifying that power extraction from the input wave is happening. It can be observed that the impact of the variation in the modulation signal at the positive and negative peaks is reflected in the current from the WEC drive. The same effect is seen in the bus voltage as well in Figure 4.9. The frequency of these signals is twice the wave frequency period because of the positive and negative peaks of the input wave. The bus voltage is also achieving the reference bus voltage value at 200V (section 2.3.3).
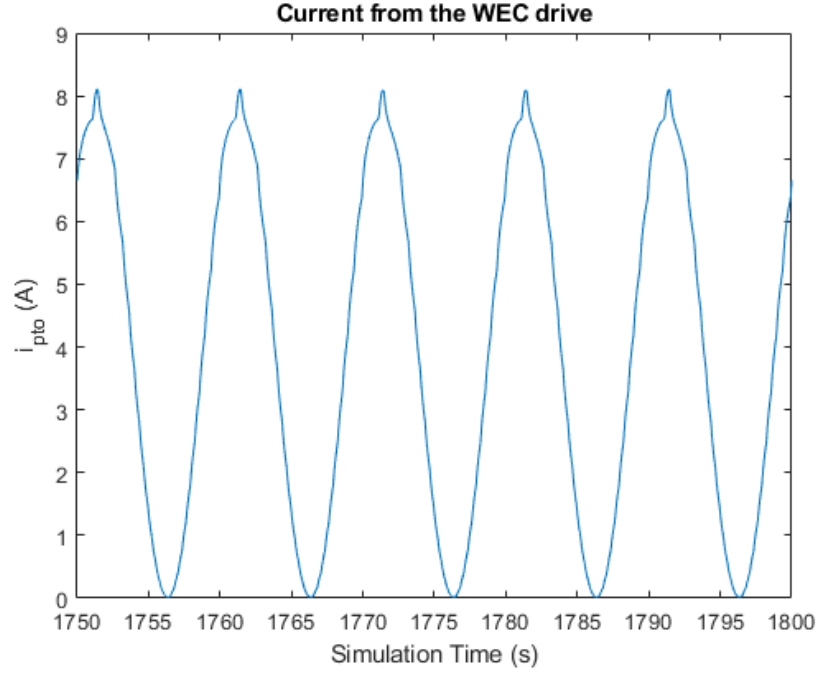
45

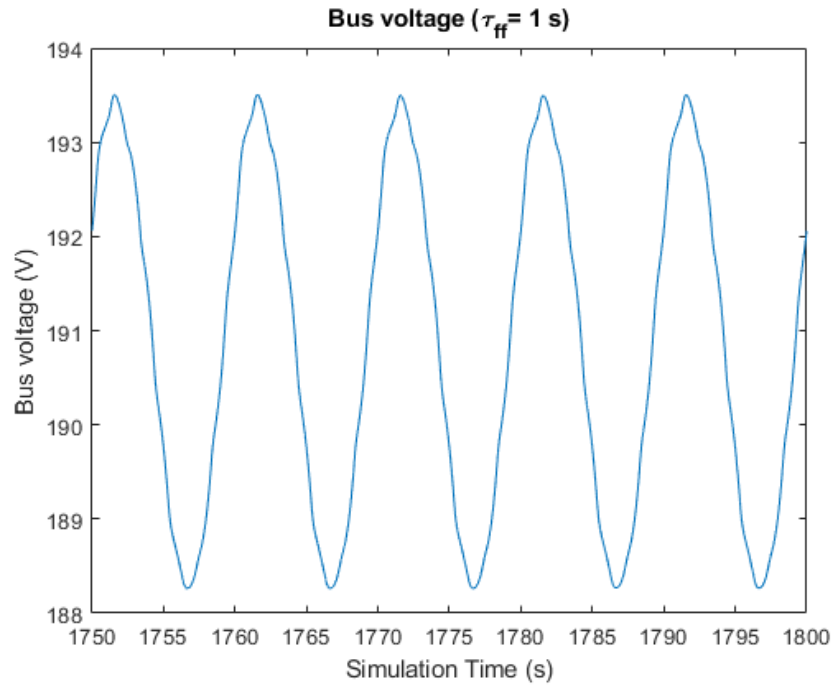**Figure 4.8:** Current from the WEC drive - single frequency

Figure 4.9: Bus voltage for $\tau_{ff} = 1$ s case - single frequency

The power flow in the WEC system is illustrated in Figure 4.10. It can be observed that the mechanical power is the highest. As the power flows in the system from the mechanical end to the grid, several losses are happening due to the parasitic elements. The peak mechanical power generated for this case is close to 1600 W and it reduces to 1300 W at grid.
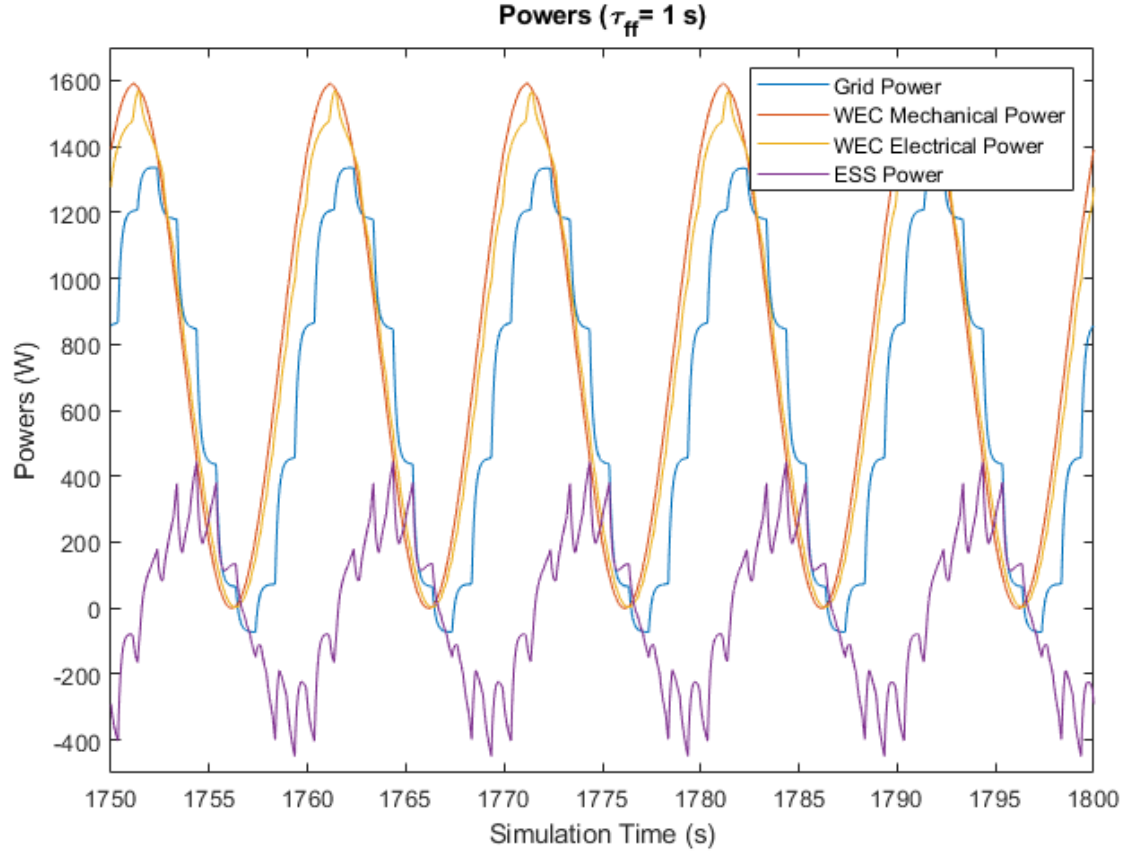

Figure 4.10: Powers in the WEC system for $\tau_{ff} = 1$s - single frequency

Similarly, Figure 4.11 shows the current flows in the WEC system. The reference grid current is updated as per the update rate. The WEC supplies the grid current/exporting power as per the reference current. It can also be observed that as per the grid reference current, the ESS is charging and discharging.
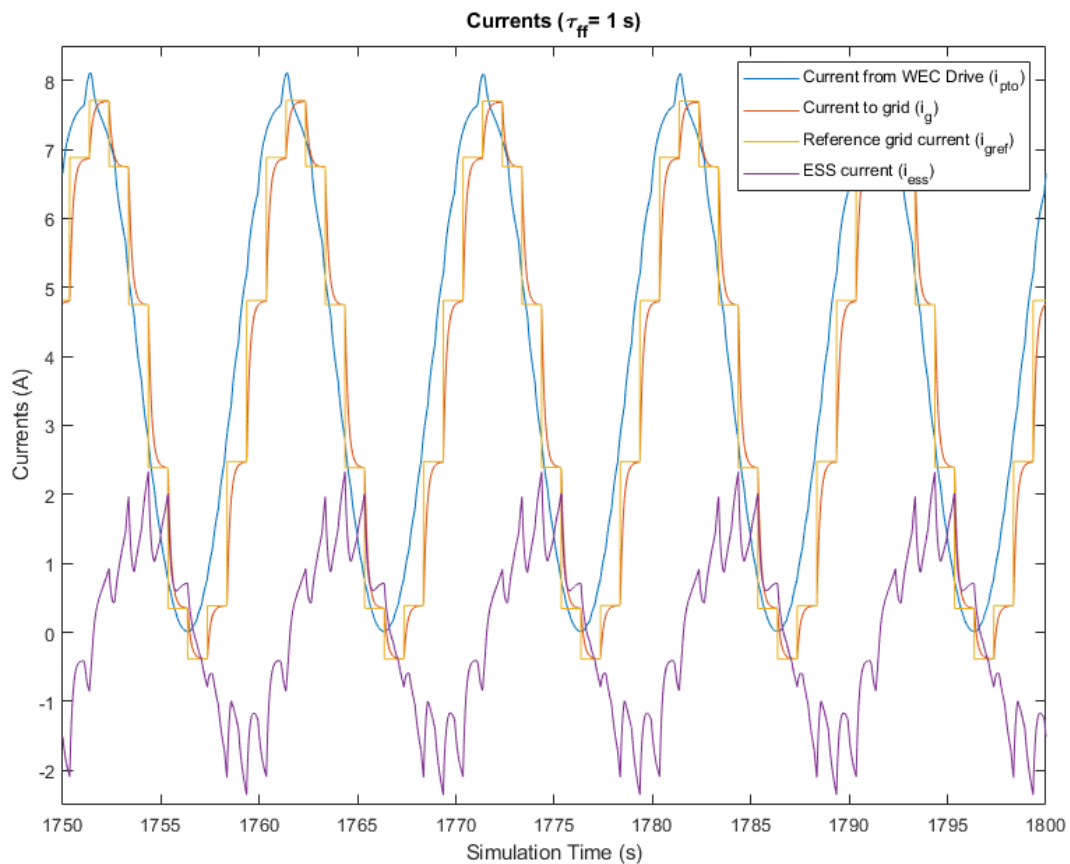

Figure 4.11: Currents in the WEC system for $\tau_{ff} = 1s$ - single frequency

The efficiency of the system for this case can be computed as

$$\eta = \frac{Average\ Grid\ Power}{Average\ Mechanical\ Power} = \frac{639.7760}{792.9071} = 80.69\%. \tag{4.2}$$

4.1.2 Multiple frequency wave test

The results presented in this section show the plots for all the essential WEC param-

eters for an update rate $\tau_{ff} = 1\ s$. In the real-world, most of the waves encountered

are multi-frequency waves. Hence, in this case, the sum of two waves with differ-

ent frequencies is the input to the model. For the presented case, wave forces are

$F_{w1} = 5000$ N and $F_{w2} = 3000$ N. The wave periods are 20 and 5 s respectively.

Figure 4.12 shows the linear forces on the buoy due to multi-frequency waves. F_e is

the actuator force for the provided wave input. The actuator force is a reaction force

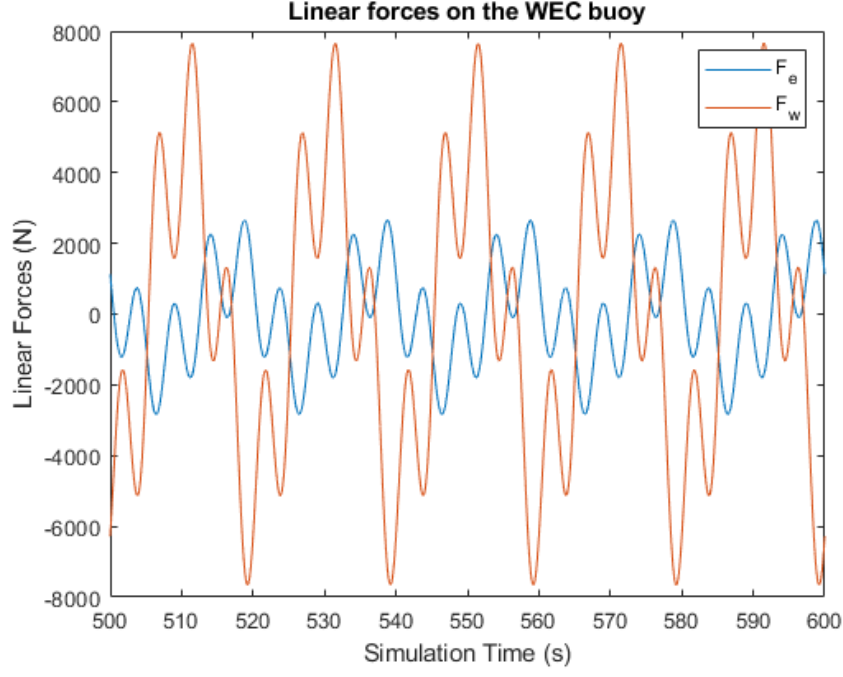to the wave input; hence, it is out of phase with the wave force.

Figure 4.12: Linear forces on the buoy - multi-frequency

Figures 4.13 and 4.14 show the vertical position and velocity of the buoy respectively for multi-frequency waves. From the reference, the buoy exhibits a vertical movement between 4.5 and -4.5 m. At the highest and lowest position, the velocity of the buoy becomes zero. The maximum velocity of the buoy was observed to be 2.3 m/s.
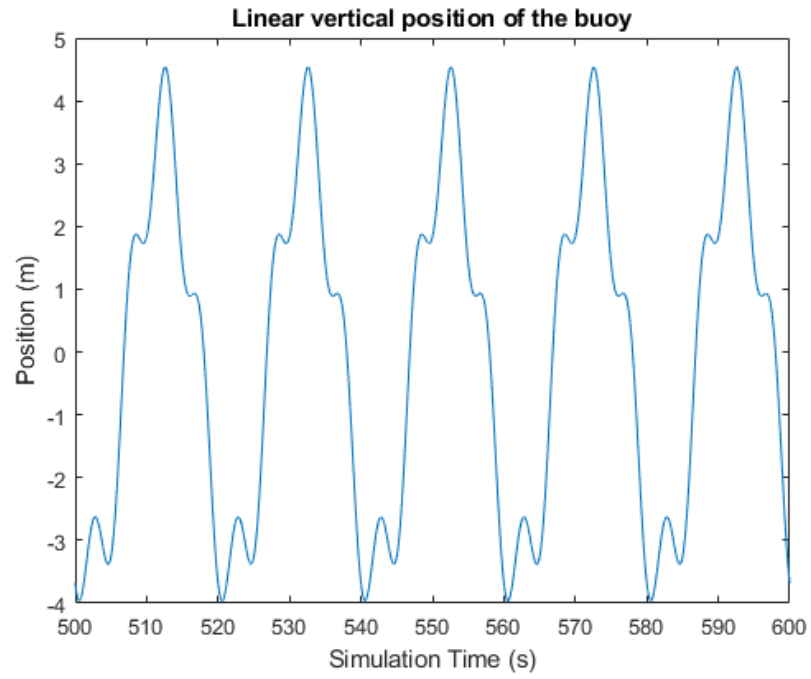
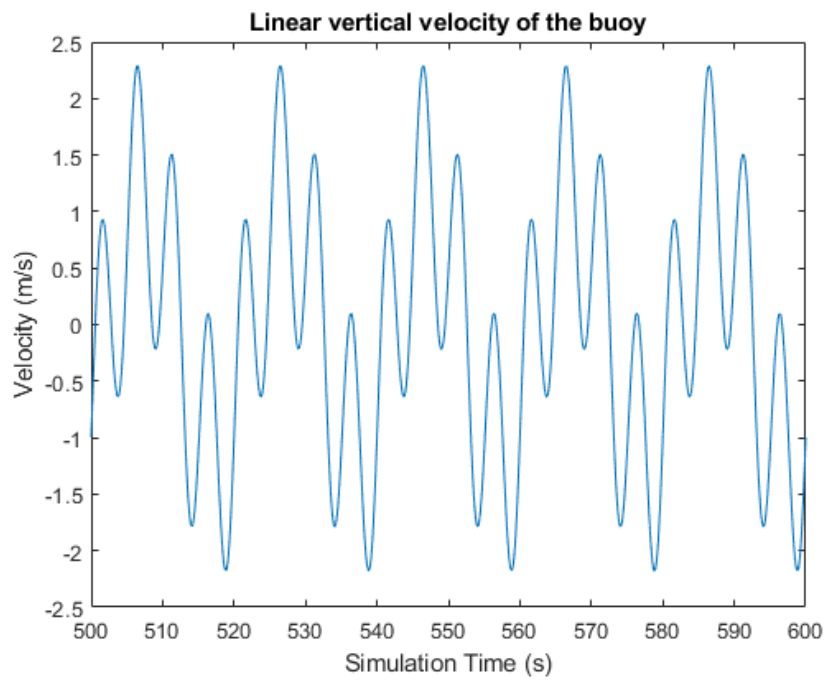**Figure 4.13:** Linear vertical position of the buoy - multi-frequency

Figure 4.14: Linear vertical velocity of the buoy - multi-frequency

51

The speed of the machine is shown in Figure 4.15. It can be validated using equation 2.4 to be

$$\omega_m = \frac{Vertical\ velocity\ of\ the\ buoy}{Gear\ radius} = \frac{2.3}{0.047} = 48.93 rad/s. \quad (4.3)$$
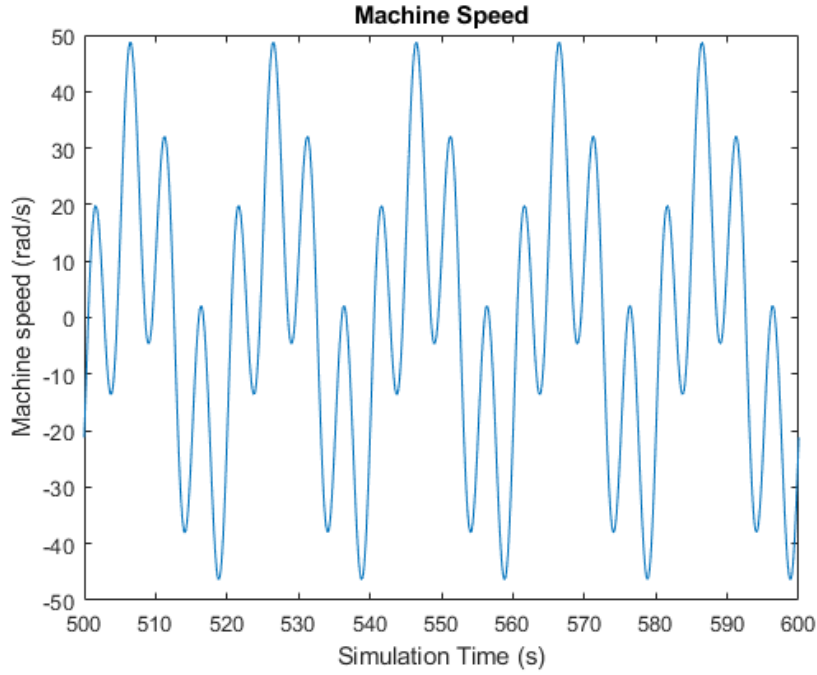

Figure 4.15: Speed of the DC machine - multi-frequency

The torque of the machine is generated through inverter PI control scheme (section 2.3.2). The reference torque generated through the reference actuator force ($F_{e,ref}$) as mentioned in section 2.3.1 can be seen in Figure 4.16. It can also be observed that the PI controller (section 2.3.2) does not have an error because the machine is achieving the reference torque. This validates that the system works well for both single and
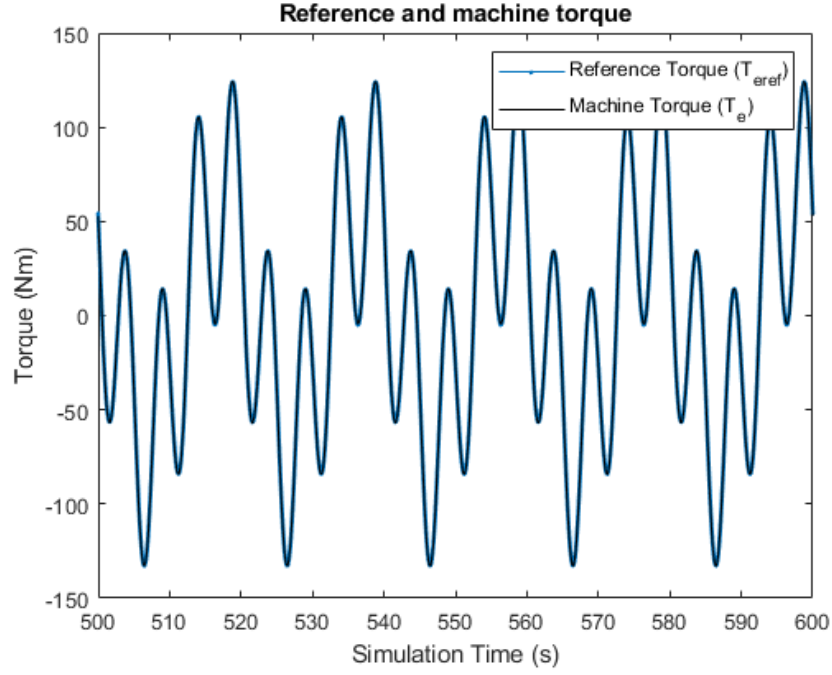
multi-frequency waves.

Figure 4.16: Reference and the actual torque of the DC machine - multi-frequency

Figure 4.17 shows the modulation signal generated by the PI controller (section 2.3.2) for the inverter control. The current from the WEC drive i_{pto} is shown in Figure 4.18 and it peaks at around 30 A for this case. The i_{pto} is always positive justifying that power extraction from the input wave is happening. It can also been observed that the output from the WEC drive increases as the input wave force increases. The frequency of these signals is twice the wave frequency period because of the positive and negative peaks of the input wave.
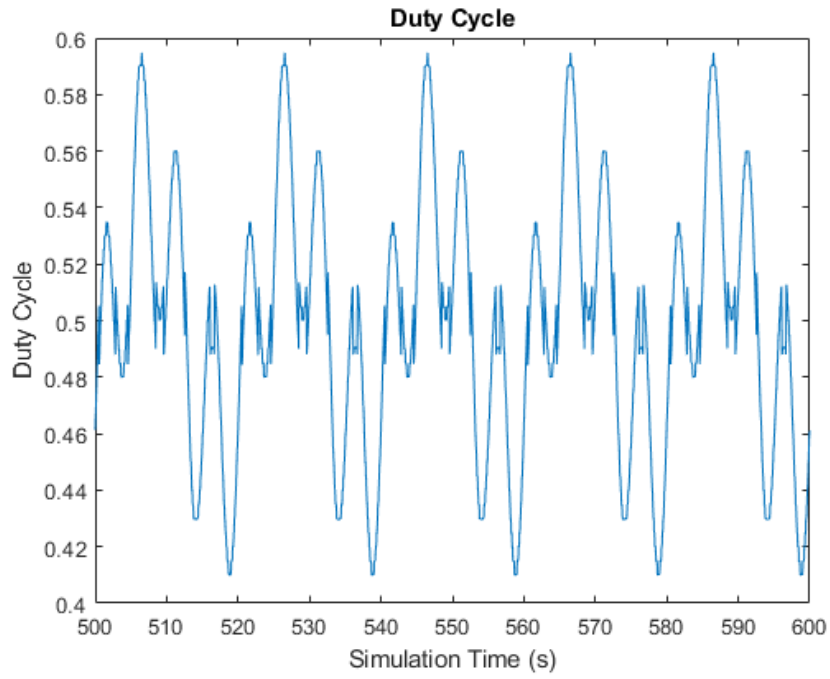
Figure 4.17: Modulation signal for inverter control - multi-frequency
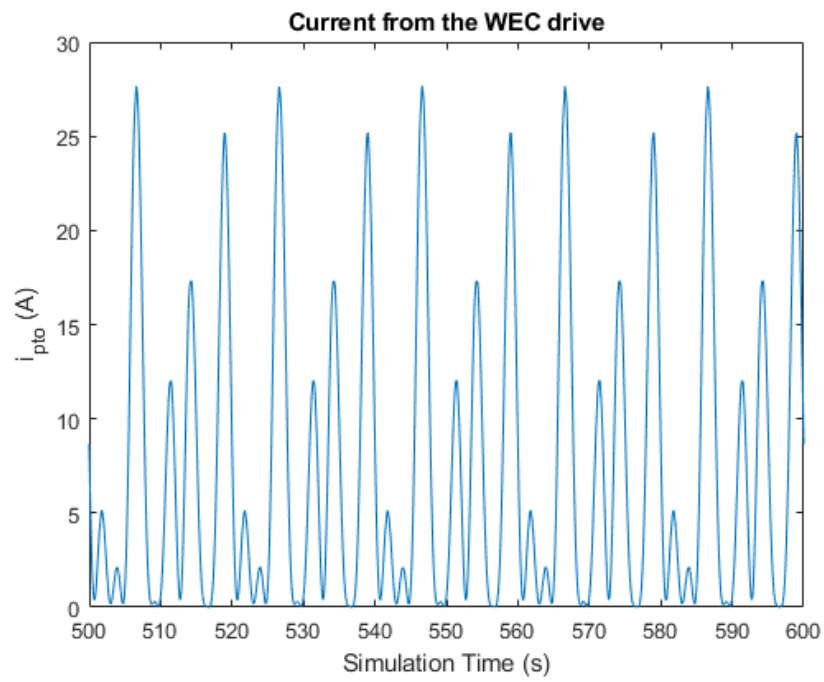

Figure 4.18: Current from the WEC drive - multi-frequency

54

Figure 4.19 shows the bus voltage for this case. The bus voltage is achieving the reference bus voltage value at 200V (section 2.3.3).
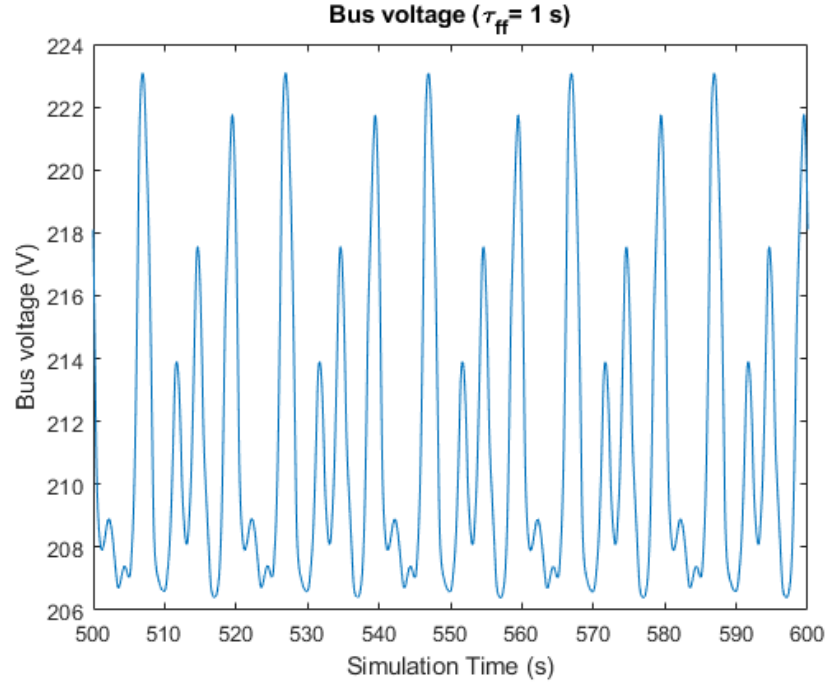

Figure 4.19: Bus voltage for $\tau_{ff} = 1$ s case - multi-frequency

The power flow in the WEC system is illustrated in Figure 4.20. It can be observed that the mechanical power is the highest. As the power flows in the system from the mechanical end to the grid, several losses are happening due to the parasitic elements. The peak mechanical power generated for this case is close to 6500 W and it reduces to 4000 W at grid. It was observed that the losses are comparatively high for the multi-frequency wave case.
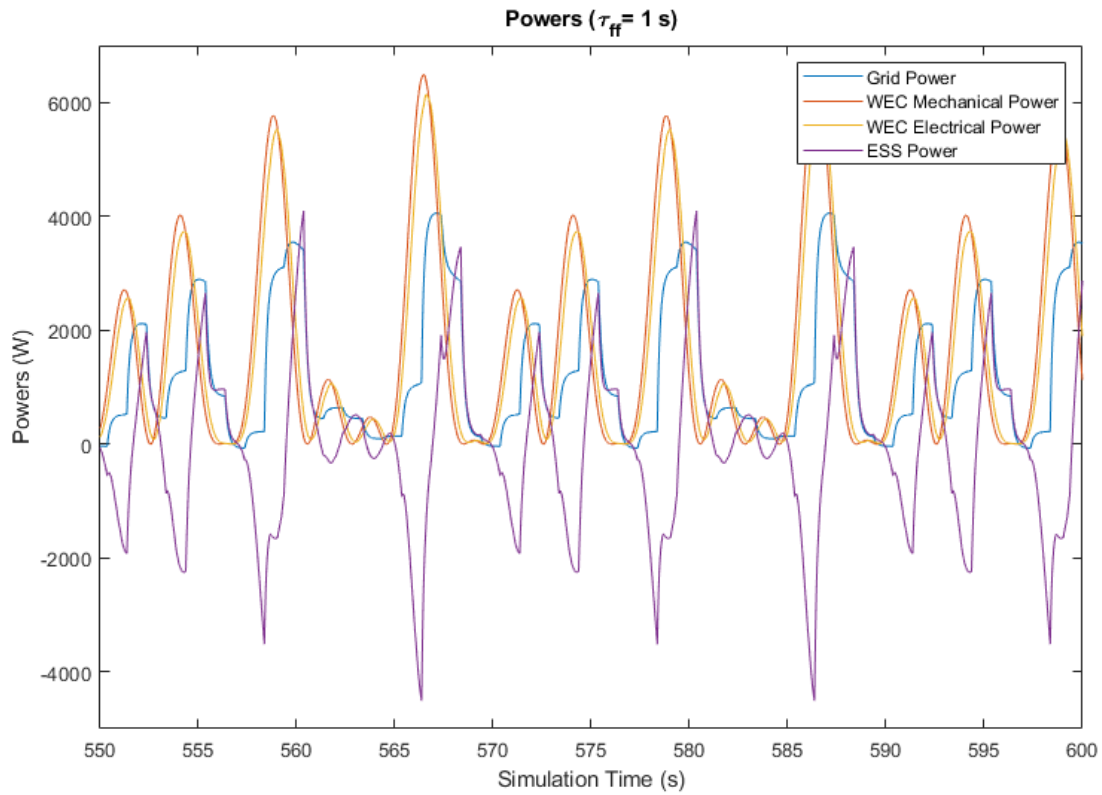

Figure 4.20: Powers in the WEC system for $\tau_{ff} = 1$ s - multi-frequency

Figure 4.21 shows the current flows in the WEC system for multi-frequency wave case. It can be observed that when the demand from the grid is low, ESS is charging using the WEC drive current and vice-e-versa.

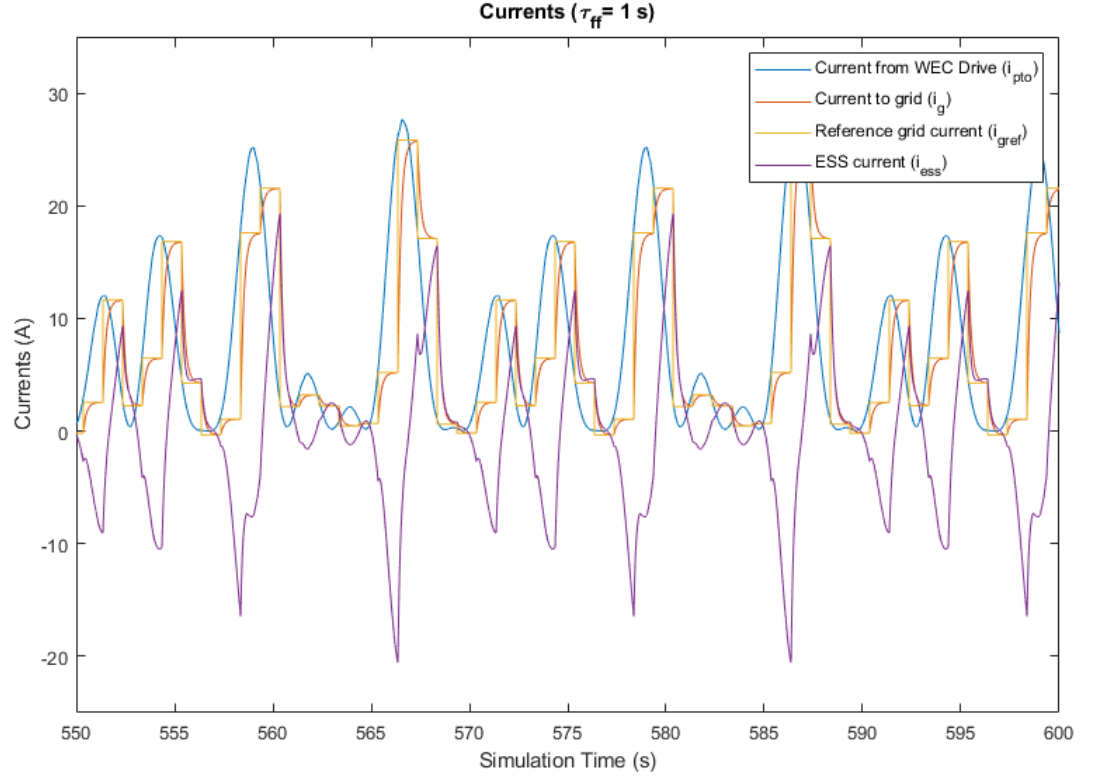**Figure 4.21:** Currents in the WEC system for $\tau_{ff} = 1$ s - multi-frequency

The efficiency of the system for this case can be computed as

$$\eta = \frac{Average\ Grid\ Power}{Average\ Mechanical\ Power} = \frac{1254.3}{1662.5} = 75.45\%. \tag{4.4}$$

The efficiency of the system during the multi-frequency test was observed to be lower

due to higher losses as compared to the single frequency test.

4.2 Operating conditions of current model based on the update rate

As mentioned earlier in section 2.3.3, the update rate is an important parameter to be explored, and a zero-order hold was used to simulate it. To study the effect of the update rate on the system, the WEC was run with the single frequency wave (section 4.1.1) for different update rates.

The wave force for the presented case (F_w) is 5000 N and the wave period is 20 s. Figure 4.22 shows the trend of the bus voltage with respect to (w.r.t) to update rates.
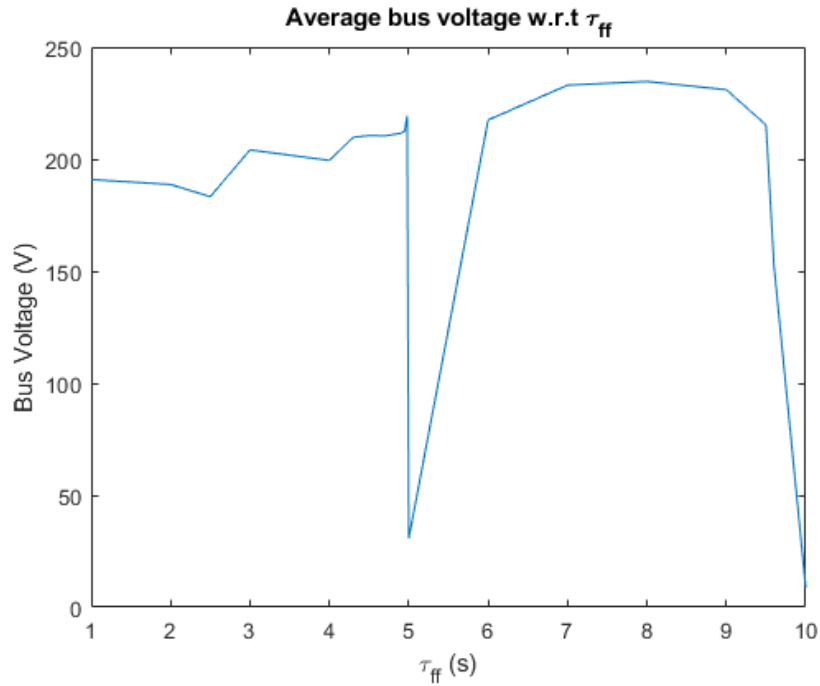

Figure 4.22: Bus voltage trend w.r.t update rate - 20 s wave period

It was observed that the system was not achieving the reference bus voltage and reaching steady state for the cases where $\tau_{ff} = 5$ s and as the update rate reaches close to 10 s. For all the other cases, the bus voltage achieves the reference bus voltage (Figure 4.22).

The variation observed here can be due to the limitation of the system while updating the grid reference current using the zero order hold. These probable reasons for the trends have been mentioned in detail later in section 4.2.1.

To validate that the result at $\tau_{ff} = 5$ s is not an outlier, data runs were done at several τ_{ff}'s close to 5 s. Data was acquired for τ_{ff} of 4.3, 4.5, 4.7, 4.9, 4.95 and 4.98 s. For all these cases, the system was attaining steady-state but, it was observed that as the update rate increases the variation in average bus voltage suddenly increases after 4.95 s and then dips at 5 s. So, this shows that the system does not achieve steady state in this case. Similar trend is seen after 9.5 s. (Figure 4.23).

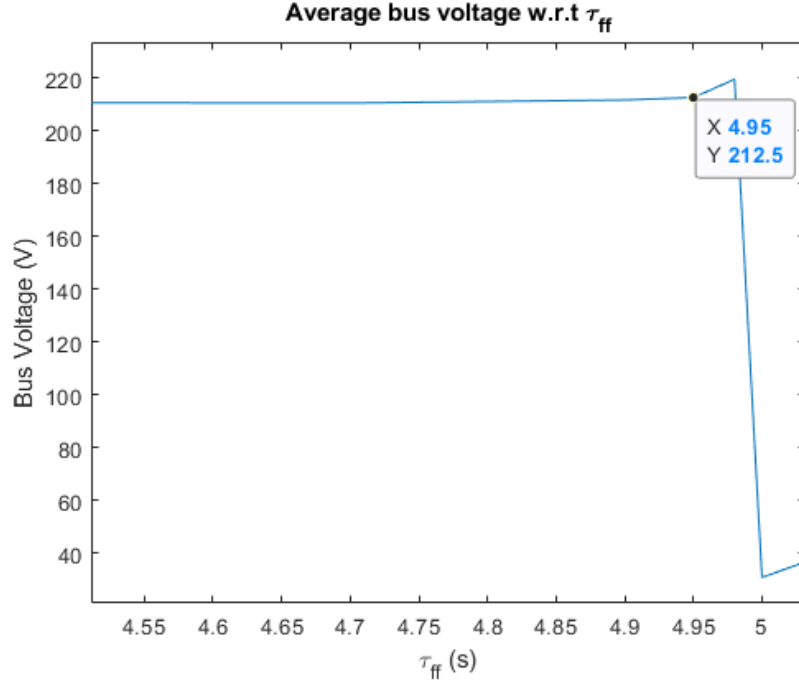**Figure 4.23:** Bus voltage trend w.r.t update rate close to 5 s - 20 s wave period

As the update rate increases, the system efficiency is reducing (Figure 4.24). The maximum efficiency at 81.51 % was observed at the update rate of 2.5 s. The efficiency is seen to be reduced after 4.95 s (Figure 4.25) because the system is not in steady state as it approaches to 5 s as seen earlier due to the operating limitation (section 4.2.1).
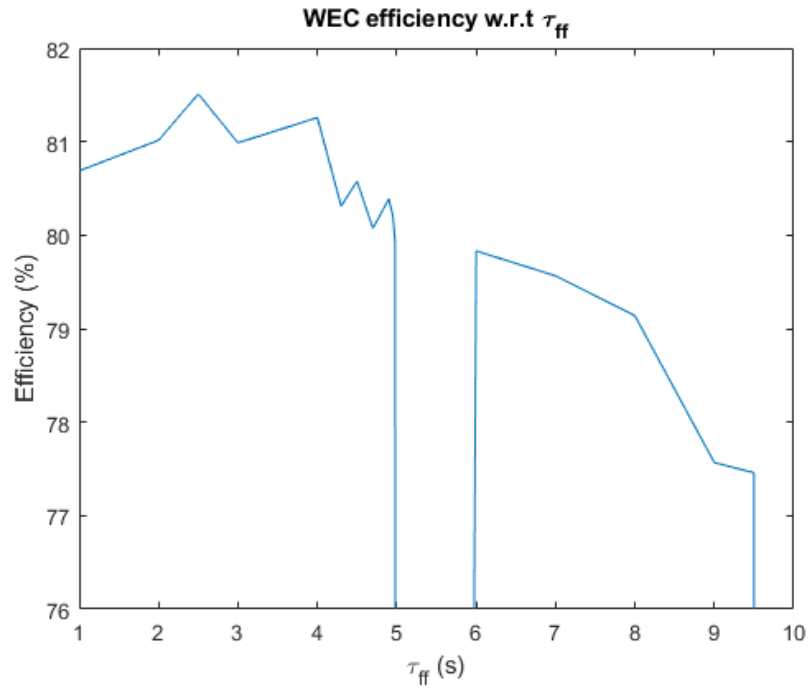
Figure 4.24: Efficiency w.r.t update rate - 20 s wave period
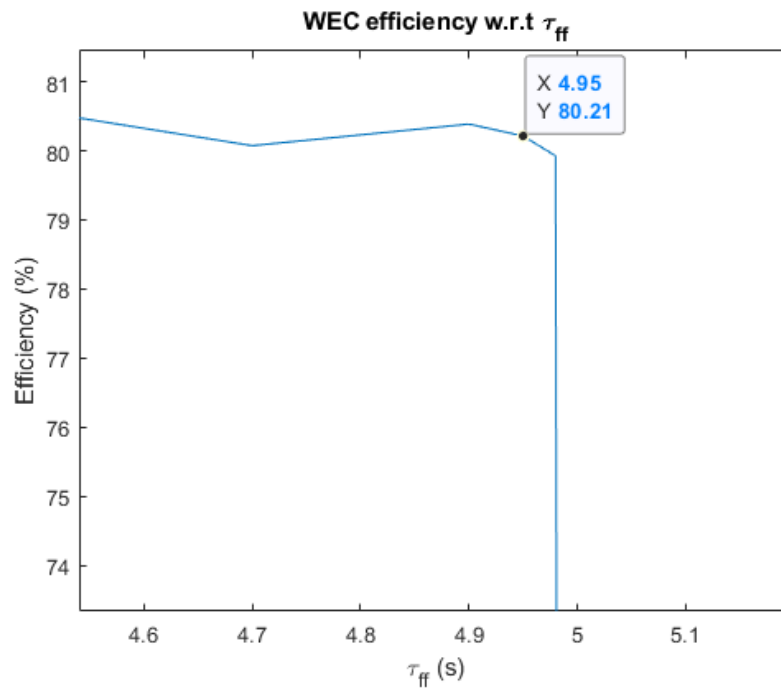
Figure 4.25: Efficiency w.r.t update rate close to 5 s - 20 s wave period

At higher update rates, the ESS power and energy are higher. This indicates that the ESS capacity should be higher because as the update rate increases, during the grid current update, the power contributed by the ESS to the grid needs to be higher (Figures 4.26 and 4.27). It should be noted that similar variations at update rate close to 5 s can be seen because it is an operating condition encountered in the system configuration.

Figure 4.26: Max ESS power w.r.t update rate - 20 s wave period
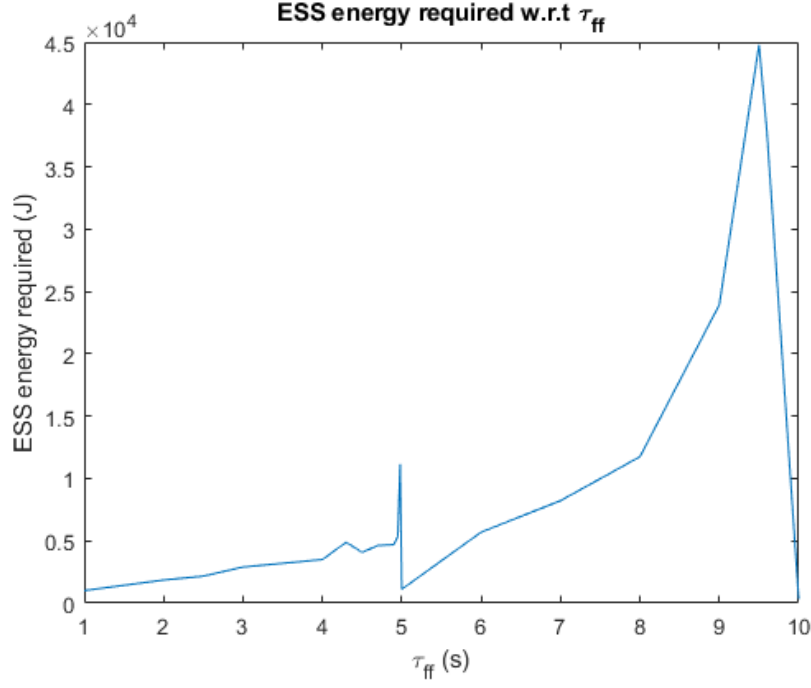
Figure 4.27: ESS energy required w.r.t update rate - 20 s wave period

4.2.1 Discussions about the operating condition of the current model

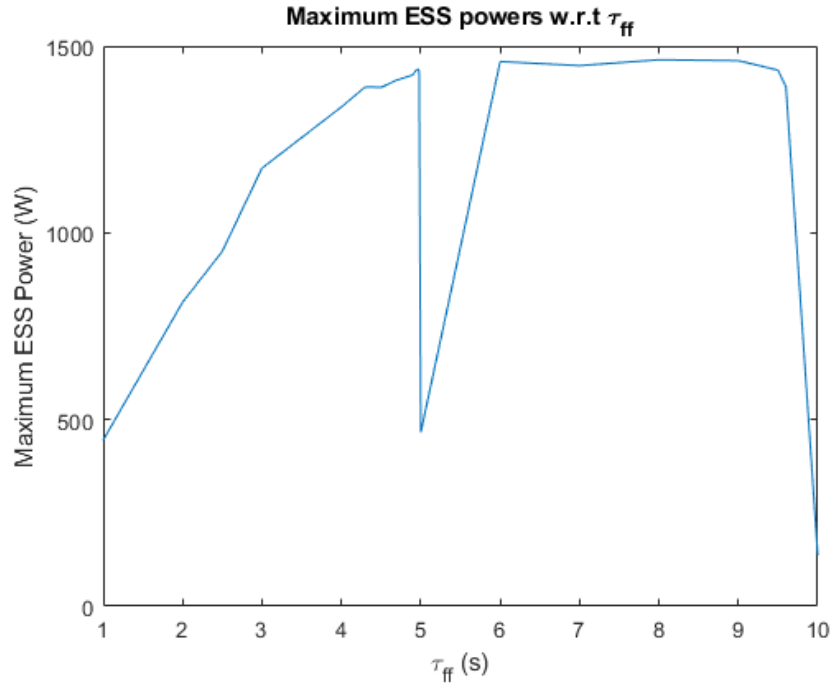The update rate is simulated using a zero-order hold as mentioned earlier. The grid reference current is computed in real-time using (2.24) and the zero-order hold samples through the data in real-time to set and hold a value for τ_{ff} s. But, when the update rate is a multiple of the wave period, due to sampling at the same point, the grid reference current value will be the same as shown in Figure 4.28 and hence, the power export will be low always though there is enough WEC drive current. This condition is a limitation in the present system configuration and needs to be explored

further.
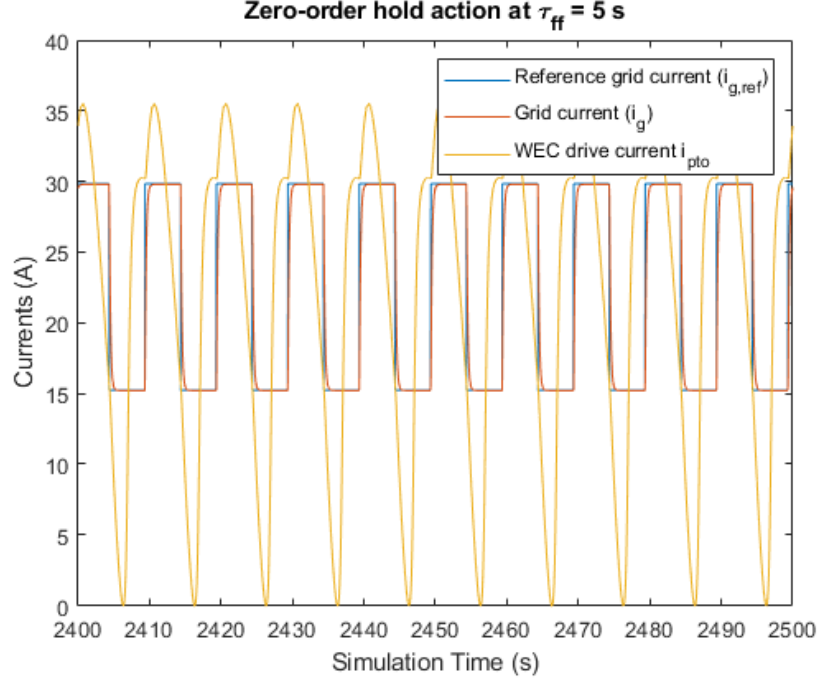
Figure 4.28: Currents at $\tau_{ff} = 5$ s

It was also observed that the system does not attain steady state when the update

rate approaches

$$\tau_{ff} \to \frac{Wave\,period}{2}. \tag{4.5}$$

This can be explained using the Nyquist criterion. As an update rate is basically

sampling a signal, the sampling frequency should be at least twice the wave frequency

for proper reconstruction.

When there are multi-frequency waves, the possibility of periodicity significantly re-

duces. Hence the observation about the stability based on the update rate due to

sampling may be less relevant when there are multiple frequency components in the wave as encountered in real-world scenarios.

4.3 ESS energy requirement

Figure 4.29 shows the ESS energy trend at steady state for both single and multi-frequency wave tests at update rate $\tau_{ff} = 1$ s. During the runs, the ESS was modeled as a supercapacitor. The supercapacitor ratings were C = 1 F and R = $0.2e^{-3}$ Ω.
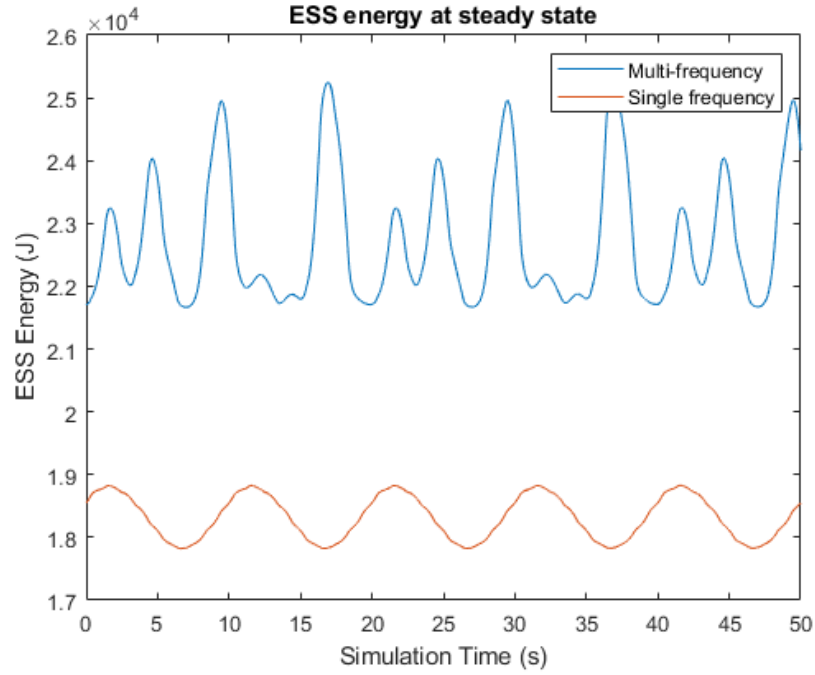
Figure 4.29: Comparing ESS energy for single and multi-frequency tests

ESS energy required during the single frequency wave test for a wave force (F_w) is 5000 N and the wave period is 20 s at the update rate of 1 s was 1004.2 J.

ESS energy required during the multi-frequency wave test for the wave forces of $F_{w1} = 5000$ N and $F_{w2} = 3000$ N and wave periods being 20 and 5 s respectively for

an update rate of 1 s was 3585.5 J.

It was observed that the ESS requirement for these cases were low. But, as the wave

force increases, the ESS energy required also increases.

Chapter 5

Conclusion and Future Work

A WEC model was developed, and a few HIL simulations were run to validate the model's working. The modeled system behaves reasonably well for single and multi-frequency waves. The efficiency of the system for the single frequency and multi-frequency test at update rate of 1 s was found to be 80.69% (4.2) and 75.45% (4.4) respectively.

The effect of the update rate on the WEC behavior for a single frequency wave was explored. The behavior exhibited a few variations when the update rate value was approaching half the wave period. It can be explained using Nyquist criterion as the sampling frequency should be at least twice the wave frequency for proper reconstruction of the grid reference current. Similarly, the system also exhibits a

69

limitation when the update rate is a multiple of the wave period probably due to periodicity in a single-frequency wave case. The limits and operating condition of the system needs further exploration.

A comparison of ESS energy requirement for both single and multi-frequency waves was presented. The ESS requirements of the system were found to be small in these preliminary tests. Further exploration in terms of multi-frequency tests and the effect of ESS on efficiency needs to be explored.

The future scope of the work is vast. This model can act as a starting point for all the studies regarding any WEC component. These improvements can be effortlessly integrated into this model, tested, and validated using the HIL devices. Modeling and design is the most important paramater to get started with HIL testing of any system. The systematic modeling of the system with appropriate I/O calibration is significant. Testing of these systems can be done on different scales from validating the model using HIL devices to replacing the individual sub-systems with hardware.

References

[1] S. Kolosok, I. Myroshnychenko, H. Mishenina, and I. Yarova, "Renewable energy innovation in europe: Energy efficiency analysis," in *E3S Web of Conferences*, vol. 234. EDP Sciences, 2021, p. 00021.

[2] J. Dashwood, "4. the outlook for energy: A view to 2040," *Australia's Energy Options: Renewables and efficiency*, p. 45, 2012.

[3] F. Taveira-Pinto, G. Iglesias, P. Rosa-Santos, and Z. D. Deng, "Preface to special topic: marine renewable energy," *Journal of Renewable and Sustainable Energy*, vol. 7, no. 6, p. 061601, 2015.

[4] "Global status report 2021," https://www.ren21.net/wp-content/uploads/2019/05/GSR2021_Full_Report.pdf, REN 21.

[5] D. Clemente, P. Rosa-Santos, and F. Taveira-Pinto, "On the potential synergies and applications of wave energy converters: A review," *Renewable and*

Sustainable Energy Reviews, vol. 135, p. 110162, 2021. [Online]. Available: https://www.sciencedirect.com/science/article/pii/S1364032120304536

[6] M. Bacic, S. Neild, and P. Gawthrop, "Introduction to the special issue on hardware-in-the-loop simulation," *Mechatronics*, vol. 19, no. 7, pp. 1041–1042, 2009.

[7] R. Isermann, J. Schaffnit, and S. Sinsel, "Hardware-in-the-loop simulation for the design and testing of engine-control systems," *Control Engineering Practice*, vol. 7, no. 5, pp. 643–653, 1999. [Online]. Available: https://www.sciencedirect.com/science/article/pii/S0967066198002056

[8] H. K. Fathy, Z. S. Filipi, J. Hagena, and J. L. Stein, "Review of hardware-in-the-loop simulation and its prospects in the automotive area," in *Modeling and simulation for military applications*, vol. 6228. International Society for Optics and Photonics, 2006, p. 62280E.

[9] "Documentation - typhoon hil," https://www.typhoon-hil.com/documentation/.

[10] W. W. Weaver, D. G. Wilson, A. Hagmuller, M. Ginsburg, G. Bacelli, R. D. Robinett, R. Coe, and Budi, "Super capacitor energy storage system design for wave energy converter demonstration," in *2020 International Symposium on Power Electronics, Electrical Drives, Automation and Motion (SPEEDAM)*, 2020, pp. 564–570.

[11] W. W. Weaver, A. Hagmuller, M. Ginsburg, D. G. Wilson, G. Bacelli, R. D. Robinett, R. Coe, and B. Gunawan, "Wec array networked microgrid control design and energy storage system requirements," in *OCEANS 2019 MTS/IEEE SEATTLE*.   IEEE, 2019, pp. 1–6.

[12] D. Wilson, G. Bacelli, R. G. Coe, D. L. Bull, O. Abdelkhalik, U. A. Korde, and R. D. Robinett III, "A comparison of wec control strategies," *Sandia National Laboratories Tech. Rep. SAND2016-4293*, vol. 10, p. 1431291, 2016.

[13] "Implement zero-order hold sample period - simulink," https://www.mathworks.com/help/simulink/slref/zeroorderhold.html.